

A variational minimization formulation for hydraulically induced fracturing in elastic-plastic solids

Daniel Kienle^{*}, Marc-André Keip

Institute of Applied Mechanics
Department of Civil and Environmental Engineering
University of Stuttgart, Stuttgart, Germany

Abstract. A variational modeling framework for hydraulically induced fracturing of elastic-plastic solids is developed in the present work. The developed variational structure provides a global minimization problem. While fracture propagation is modeled by means of a phase-field approach to fracture, plastic effects are taken into account by using a Drucker–Prager-type yield-criterion function. This yield-criterion function governs the plastic evolution of the fluid-solid mixture. Fluid storage and transport are described by a Darcy–Biot-type formulation. Thereby the fluid storage is decomposed into a contribution due to the elastic deformations and one due to the plastic deformations. A local return mapping scheme is used for the update of the plastic quantities. The global minimization structure demands a $H(\text{div})$ -conforming finite-element formulation. Furthermore this is combined with an enhanced-assumed-strain formulation in order to overcome locking phenomena arising from the plastic deformations. The robustness and capabilities of the presented framework will be shown in a sequence of numerical examples.

Keywords: Variational principles, porous media, ductile fracture, hydraulic fracture, phase-field modeling.

1 Introduction

One of the main applications for a model of hydraulically induced fractures can be found in the recently utilized oil-production technique called fracking. During this process a highly pressurized fluid is injected into a perforated bore hole. The goal is to induce fractures in layers of the earth’s crust that store large amounts of oil and gas. The fractures are created to increase the fluid permeability of the present soil or rock, therewith leading to a higher flow of gas and oil into the bore hole where it is collected. The main criticisms of this technique are related to the inducement of fractures that could lead to environmental issues such as seismic activities or contamination of drinking water. Therefore,

^{*}Corresponding author. *E-mail address:* kienle@mechbau.uni-stuttgart.de

in recent years various attempts have been made to better capture and understand the underlying physical processes, for example by the development of models that can be used in numerical simulations. The idea is that an accurate and robust model can help in forecasting both risks and potential of such a technique. To be successful, such a model has to capture three distinct mechanisms: First, it has to describe the mechanical deformation of the present porous medium (which could be soil or rock); second, it has to describe the fluid transport throughout the intact and fractured porous medium; third, the model needs to be capable of describing fracture initiation and propagation, for example driven by fluid pressure.

To embed the present work into the literature, we comment on recent development in the field. For the modeling of hydraulic fracturing, it is of substantial importance to describe the mechanical deformation of the underlying porous media. Powerful techniques in this direction are given on the one hand by model formulations within the context of the so-called Theory of Porous Media, see [de Boer \[2000\]](#), [Ehlers \[2002\]](#) and [Bluhm and De Boer \[1997\]](#). An alternative approach that is suitable for the description of fully saturated porous media with one fluid phase is formulated in the seminal works of [Terzaghi \[1925\]](#) and [Biot \[1941\]](#). Associated models reside in the area of the Biot theory of consolidation, see [Detournay and Cheng \[1993\]](#) and [Bear \[1972\]](#) for a general overview.

When it comes to the modeling of fluid flow within a porous medium, it is often made use of the law of [Darcy \[1856\]](#). Darcy's law provides a phenomenological approach to the modeling of fluid flux that is driven by gradients of fluid pressure or, more precisely, by gradients of the chemical potential. Darcy's law is often referred to as a macroscopic approach since it describes the fluid flow through the porous medium's pore scale in an averaged or homogenized sense. Fluid flow within fractures, i.e. regions without solid content, could directly be modeled based on the Navier–Stokes-equation. Associated simplifications can be based on the lubrication theory and lead to so-called Poiseuille-type flow models. While the first approach is often used in combination with models related to the Theory of Porous Media, the latter one can nicely be embedded in formulations that relate to Biot's theory of consolidation.

Since the present work aims at the description of fracturing processes in porous media, we briefly refer to some related literature. Fundamental concepts for the description of fracture were proposed by [Griffith \[1921\]](#) and [Irwin \[1958\]](#). These works provide energy-based fracture criteria for brittle materials and build the theoretical basis for the recently developed phase-field models of fracturing. With regard to the latter we highlight the contributions of [Francfort and Marigo \[1998\]](#), [Bourdin et al. \[2000, 2008\]](#), [Amor et al. \[2009\]](#), [Kuhn and Müller \[2010\]](#), [Miehe et al. \[2010a\]](#) and [Pham et al. \[2011\]](#). The phase-field approach to fracture is extremely versatile and has been extended to the modeling of duc-

tile fracture (Miehe et al. [2015a, 2016a,b,c], Ambati et al. [2015], Borden et al. [2016], Alessi et al. [2018a], Steinke et al. [2020], Yin and Kalske [2020]), anisotropic fracturing (Li et al. [2015], Teichtmeister et al. [2017], Storm et al. [2020]) and fatigue fracture (Alessi et al. [2018b], Lo et al. [2019], Schreiber et al. [2020], Carrara et al. [2020]), just to name a few.

Next to the above mentioned extensions, the phase-field approach to fracture has also seen pronounced activity in the field of porous media. Here we highlight the contributions of Mikelic et al. [2015a,c,b], Miehe et al. [2015b], Wilson and Landis [2016], Wu and De Lorenzis [2016], Mauthe and Miehe [2017] and Cajuhi et al. [2018] that are embedded into Biot’s theory of consolidation. In that connection we also mention a recent work on the numerical treatment of poro-elastic problems, in which an emphasis is put on suitable finite-element formulations Teichtmeister et al. [2019]. Combinations of the Theory of Porous Media with the phase-field approach to fracture have been provided by Ehlers and Luo [2017, 2018a,b]; Heider and Markert [2017].

We note that the above mentioned models all relate to elastic deformations of the material. However, there is experimental evidence that elastic material response alone cannot capture all relevant effects Johnson et al. [1991]. This serves as a motivation to the develop models that incorporate elastic-plastic deformations. Here we would like to refer to the recent developments of Pise et al. [2019] and Aldakheel et al. [2020]. In the given works, the plastic response is incorporated by introducing a Drucker–Prager-type yield criterion function Drucker and Prager [1952]. We note that the works Pise et al. [2019], Aldakheel et al. [2020] are not variational and consider a yield-criterion function in terms of the effective stresses. The present work provides an alternative formulation of elastic-plastic hydraulic fracturing in a rigorously variational setting motivated by the ideas of Armero [1999]. In the latter work, an additive split of the fluid content into an elastic and a plastic part is suggested, which leads to a constitutive fluid pressure as a function of only elastic quantities. This concept is perfectly suitable for a variational framework that combines the elastic-plastic deformation of the porous medium with the fluid transport on the one hand and the fracture initiation and evolution on the other.

The present work is structured as follows. In Section 2 the unknown fields and associated kinematic relations are introduced. Thereafter, in 3, we provide the variational framework and the constitutive functions. Here, we make use of a Darcy–Biot-type formulation for the fluid transport in the porous medium and a Drucker–Prager-type yield-criterion function for plastic flow. This then leads to the set of Euler equations that describe the behavior of a fracturing porous-elastic-plastic solid. The numerical treatment of the problem is based on a time-discrete incremental variational formulation combined with a local return-mapping scheme and discussed in Section 4. We showcase the capabilities of

the presented numerical framework for hydraulically induced fracturing of porous-elastic-plastic solids by means of some numerical examples to be discussed in Section 5. In detail we consider a rigid-footing test as well as two fluid-injection tests. A summary and an outlook will be provided in Section 6.

2 Independent and primary fields

In the present section we introduce the independent and primary fields of the porous-elastic-plastic fracture model. They account for the elastic-plastic deformation of a body \mathcal{B} , for the fluid flux and storage in \mathcal{B} as well as for the fracture initiation and evolution in \mathcal{B} . The surface of the body will in the following be denoted as $\partial\mathcal{B}$.

Small-strain kinematics. The model presented in this work is formulated in the context of the infinitesimal-strain theory. Hence, we consider the displacement field $\mathbf{u}(\mathbf{x}, t)$ at the material point $\mathbf{x} \in \mathcal{B}$ and time t

$$\mathbf{u} : \begin{cases} \mathcal{B} \times \mathcal{T} \rightarrow \mathcal{R}^3 \\ (\mathbf{x}, t) \mapsto \mathbf{u}(\mathbf{x}, t) \end{cases} \quad (1)$$

as independent field. Based on that, we introduce the infinitesimal strain tensor as a primary variable. It can be computed from the displacement gradient by

$$\boldsymbol{\varepsilon} := \frac{1}{2}(\nabla\mathbf{u} + \nabla\mathbf{u}^T). \quad (2)$$

Plastic deformations. Since we are interested in modeling ductile response of the material, we additively decompose the strain tensor (3) into elastic and plastic contributions

$$\boldsymbol{\varepsilon} = \boldsymbol{\varepsilon}^e + \boldsymbol{\varepsilon}^p, \quad (3)$$

wherein the plastic strain $\boldsymbol{\varepsilon}^p$ will be treated as a local internal variable. Further, to describe local isotropic hardening, we introduce a local hardening field α formally by

$$\alpha : \begin{cases} \mathcal{B} \times \mathcal{T} \rightarrow \mathcal{R} \\ (\mathbf{x}, t) \mapsto \alpha(\mathbf{x}, t). \end{cases} \quad (4)$$

Fluid mass and fluid flux. The initial density (mass per unit volume) of the fluid-solid mixture is denoted by m_0 . It can be computed from the densities of the fluid ρ_f and

the solid ρ_s through the given porosity of the mixture φ as

$$m_0 = \rho_f \varphi + \rho_s (1 - \varphi) \quad \text{with} \quad \varphi = \frac{V_{\text{pore}}}{V_{\text{pore}} + V_{\text{solid}}}. \quad (5)$$

In the above equation, the porosity φ has been obtained from the given pore and solid volume V_{pore} and V_{solid} , respectively. The sum of solid and fluid volume is often denoted as bulk volume V_{bulk} .

Following Biot's approach to thermodynamically open systems, the mass balance in its global and local representation reads (Biot [1984])

$$\frac{d}{dt} \int_{\mathcal{B}} m_0 + m \, dV = - \int_{\partial \mathcal{B}} \mathfrak{h} \cdot \mathbf{n} \, dA \quad \Leftrightarrow \quad \dot{m} = - \operatorname{div} \mathfrak{h} \quad \text{in } \mathcal{B}. \quad (6)$$

Here, m denotes the change in the bulk's density, which is caused by fluid flux through the body's surface. Thus, the vector \mathfrak{h} given on the right-hand side of (6) denotes a fluid-flux vector. Formally, the latter two quantities can be introduced as

$$m : \begin{cases} \mathcal{B} \times \mathcal{T} \rightarrow \mathcal{R} \\ (\mathbf{x}, t) \mapsto m(\mathbf{x}, t) \end{cases} \quad \text{and} \quad \mathfrak{h} : \begin{cases} \mathcal{B} \times \mathcal{T} \rightarrow \mathcal{R}^3 \\ (\mathbf{x}, t) \mapsto \mathfrak{h}(\mathbf{x}, t). \end{cases} \quad (7)$$

In what follows we denote m as the change of fluid content. Analogous to the strain tensor, we decompose m into an elastic and a plastic part

$$m = m^e + m^p. \quad (8)$$

Here, the plastic contribution m^p describes a change in bulk density that is caused by plastic deformations. It is associated with fluid that is remanently squeezed out or soaked in due to plastic deformations.

Fracture phase field. As mentioned above, we will model cracks and their evolution based on the phase-field approach to fracture. The fracture phase field d is thus formally introduced as

$$d : \begin{cases} \mathcal{B} \times \mathcal{T} \rightarrow [0, 1] \\ (\mathbf{x}, t) \mapsto d(\mathbf{x}, t). \end{cases} \quad (9)$$

It denotes with $d = 0$ an intact state and with $d = 1$ a broken state of the material. The phase field is used to approximate a sharp crack interface Γ in a diffuse manner. This results in the definition of a regularized crack surface Γ_l in terms of a crack-surface density γ and a corresponding length-scale parameter l given by

$$\Gamma \approx \Gamma_l(d) := \int_{\mathcal{B}} \gamma(d, \nabla d) \, dV \quad \text{with} \quad \gamma(d, \nabla d) := \frac{1}{2l} d^2 + \frac{l}{2} |\nabla d|^2, \quad (10)$$

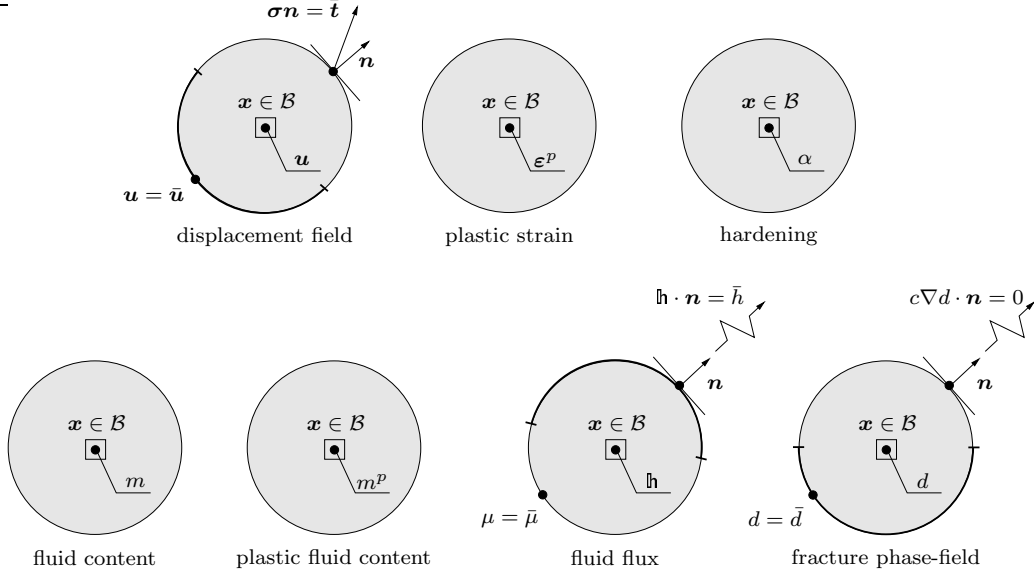


Figure 1: The unknown fields for porous-elastic-plastic solids at fracture. The boundary $\partial\mathcal{B}$ is decomposed into Dirichlet and Neumann parts for the *displacement* $\partial\mathcal{B}_u \cup \partial\mathcal{B}_t$, the *fluid flux* $\partial\mathcal{B}_h \cup \partial\mathcal{B}_\mu$ and the *fracture phase-field* $\partial\mathcal{B}_d \cup \partial\mathcal{B}_f$. For the fracture phase-field, zero Neumann boundary conditions are assumed. Here c is a constant depending on the model formulation.

Note that the sharp crack surface is recovered for vanishing length-scale parameter ($l \rightarrow 0 \Rightarrow \Gamma_l \rightarrow \Gamma$). Here we follow the notation of Miehe et al. [2010b].

3 Variational formulation of fracturing porous-elastic-plastic solids

Based on the previous section, we are able to introduce the primary fields for the description of fracturing porous-elastic-plastic solids as

$$\mathfrak{U} := \{\mathbf{u}, \mathfrak{h}, d, \boldsymbol{\varepsilon}^p, \alpha, m^p\}. \quad (11)$$

In order to formulate a rate-type variational principle we define the rate of the primary fields as

$$\dot{\mathfrak{U}} := \{\dot{\mathbf{u}}, \dot{\mathfrak{h}}, \dot{d}, \dot{\boldsymbol{\varepsilon}}^p, \dot{\alpha}, \dot{m}^p\}. \quad (12)$$

Furthermore, we identify the constitutive state of the model and its evolution as

$$\mathfrak{C} := \{\boldsymbol{\varepsilon}, m, \mathfrak{h}, d, \nabla d, \boldsymbol{\varepsilon}^p, \alpha, m^p\} \quad \text{and} \quad \dot{\mathfrak{C}} := \{\dot{\boldsymbol{\varepsilon}}, \dot{\mathfrak{h}}, \text{div } \dot{\mathfrak{h}}, \dot{d}, \nabla \dot{d}, \dot{\boldsymbol{\varepsilon}}^p, \dot{\alpha}, \dot{m}^p\}, \quad (13)$$

respectively.

3.1 Formulation of the rate-type potential

The general form of the rate-type potential is given by

$$\Pi(\dot{\mathbf{u}}; \mathbf{u}) := \frac{d}{dt} E(\dot{\mathbf{c}}; \mathbf{c}) + D(\dot{\mathbf{c}}) - P_{\text{ext}}(\dot{\mathbf{u}}), \quad (14)$$

where $\frac{d}{dt} E(\dot{\mathbf{c}}; \mathbf{c})$ is the rate of the energy, $D(\dot{\mathbf{c}})$ is the dissipation potential and $P_{\text{ext}}(\dot{\mathbf{u}})$ is the potential of the external loading. The rate of the energy is described in terms of the energy density $\psi(\mathbf{c})$

$$\frac{d}{dt} E(\dot{\mathbf{c}}; \mathbf{c}) = \frac{d}{dt} \int_{\mathcal{B}} \psi(\mathbf{c}) \, dV, \quad (15)$$

which, by application of the chain rule yields

$$\frac{d}{dt} E(\dot{\mathbf{c}}; \mathbf{c}) = \int_{\mathcal{B}} (\partial_{\varepsilon} \psi : \dot{\varepsilon} - \partial_m \psi \operatorname{div} \mathbf{h} + \partial_d \psi \dot{d} + \partial_{\varepsilon^p} \psi : \dot{\varepsilon}^p + \partial_{\alpha} \psi \dot{\alpha} + \partial_{m^p} \psi \dot{m}^p) \, dV. \quad (16)$$

In the latter equation, we made use of the fluid mass balance (6)₂. Similarly to the rate of energy the dissipation potential can be expressed in terms of a dissipation potential density $\phi(\dot{\mathbf{c}})$

$$D(\dot{\mathbf{c}}) = \int_{\mathcal{B}} \phi(\dot{\mathbf{c}}) \, dV. \quad (17)$$

Combing the right-hand sides of equations (16) and (17) yields the internal rate-potential density per unit volume

$$\pi(\dot{\mathbf{c}}; \mathbf{c}) = \partial_{\varepsilon} \psi : \dot{\varepsilon} - \partial_m \psi \operatorname{div} \mathbf{h} + \partial_d \psi \dot{d} + \partial_{\varepsilon^p} \psi : \dot{\varepsilon}^p + \partial_{m^p} \psi \dot{m}^p + \partial_{\alpha} \psi \dot{\alpha} + \phi(\dot{\mathbf{c}}). \quad (18)$$

so that

$$\Pi(\dot{\mathbf{u}}; \mathbf{u}) := \int_{\mathcal{B}} \pi(\dot{\mathbf{c}}; \mathbf{c}) \, dV - P_{\text{ext}}(\dot{\mathbf{u}}). \quad (19)$$

The particular forms of the energy density $\psi(\mathbf{c})$, the dissipation-potential density $\phi(\dot{\mathbf{c}})$ and the potential of the external loading $P_{\text{ext}}(\dot{\mathbf{u}})$ will be discussed in the following sections.

3.1.1 Constitutive energy density

The energy density has two contributions, one from the solid ψ_{solid} and one from the fluid ψ_{fluid}

$$\psi(\mathbf{c}) = \psi_{\text{solid}}(\varepsilon - \varepsilon^p, \alpha, d) + \psi_{\text{fluid}}(\varepsilon - \varepsilon^p, m - m^p). \quad (20)$$

Energy density of the solid phase. The energy density of the solid phase ψ_{solid} can be decomposed into an effective elastic and a plastic part

$$\psi_{\text{bulk}}(\boldsymbol{\varepsilon}^e, \alpha, d) = \psi_{\text{eff}}(\boldsymbol{\varepsilon}^e, d) + \psi_{\text{plast}}(\alpha, d). \quad (21)$$

Both parts depend on the fracture phase field d by means of a degradation function $g(d)$. The degraded effective elastic energy reads

$$\psi_{\text{eff}}(\boldsymbol{\varepsilon}^e, d) = [g(d) + k]\psi_{\text{eff}}^{0+}(\boldsymbol{\varepsilon}^e) + \psi_{\text{eff}}^{0-}(\boldsymbol{\varepsilon}^e), \quad (22)$$

where the superscript “0” indicates the energy density of the undamaged solid matrix. In the latter equation, we have decomposed the undamaged energy into tensile and compressive parts (indicated by the superscripts “+” and “-”, respectively), from which only the tensile part is assumed to contribute to fracture propagation. The parameter $k \ll 1$ ensures the well posedness of the problem. In what follows, we assume that $g(d) = (1-d)^2$.

The undamaged effective energies $\psi_{\text{eff}}^{0\pm}$ represent the behavior of the elastic matrix and take the simple quadratic forms

$$\psi_{\text{eff}}^{0\pm}(\boldsymbol{\varepsilon}^e) = \frac{\lambda}{2} \langle \text{tr}(\boldsymbol{\varepsilon}^e) \rangle_{\pm}^2 + G \boldsymbol{\varepsilon}_{\pm}^e : \boldsymbol{\varepsilon}_{\pm}^e \quad \text{with} \quad \boldsymbol{\varepsilon}_{\pm}^e = \sum_{i=1,3} \langle \lambda_i^e \rangle_{\pm} \mathbf{n}_i \otimes \mathbf{n}_i \quad (23)$$

in terms of the elastic strain $\boldsymbol{\varepsilon}^e$ and the Lamé constants $\lambda \geq -\frac{2}{3}G$ and $G \geq 0$. The tensile and compressive strains $\boldsymbol{\varepsilon}_{\pm}^e$ are given in terms of the eigenvalues of the strain tensor λ_i^e and the ramp function $\langle x \rangle_{\pm} = (x \pm |x|)/2$.

The plastic energy density considers isotropic saturation-type hardening and takes the form

$$\psi_{\text{plast}}(\alpha, d) = [g(d) + k]\psi_{\text{plast}}^0(\alpha) \quad \text{with} \quad \psi_{\text{plast}}^0(\alpha) = \frac{h}{2}\alpha^2 + \sigma_y \left[\alpha + \frac{1}{\omega} \exp(-\omega\alpha) - \frac{1}{\omega} \right]. \quad (24)$$

Here, $h \geq 0$ is the hardening modulus, σ_y is the saturated yield shift and ω is a saturation parameter, see [Kienle et al. \[2019\]](#). The resulting hardening function $\beta(\alpha, d) = \partial_{\alpha}\psi_{\text{plast}}(\alpha, d)$ is shown in [Figure 3](#).

Energy density of the fluid phase. Based on Biot’s theory of consolidation ([Biot \[1941\]](#)) the fluid energy density is chosen as

$$\psi_{\text{fluid}}(\boldsymbol{\varepsilon}^e, m^e) = \frac{M}{2} \left[b \text{tr}(\boldsymbol{\varepsilon}^e) - \frac{m^e}{\rho_f} \right]^2, \quad (25)$$

where M is Biot's modulus, b is Biot's coefficient and ρ_f is the fluid density. It satisfies the following conditions in terms of the fluid pressure p

$$p := -\frac{1}{b}\partial_{\text{tr}}\boldsymbol{\varepsilon}\psi_{\text{fluid}} = \rho_f\partial_m\psi_{\text{fluid}}. \quad (26)$$

We refer to Miehe et al. [2015b] for a more detailed discussion on the construction of ψ_{fluid} . Note that according to (25) and (26) the fluid pressure depends only on the elastic quantities $\boldsymbol{\varepsilon}^e$ and m^e .

3.1.2 Dissipation potential density

Similar to the energy density the dissipation potential density can be additively decomposed into individual contributions, here associated with dissipative effects arising from fluid flow, fracture evolution and plastic deformations. The dissipation potential density is formally given by

$$\phi(\dot{\boldsymbol{c}}) = \phi_{\text{fluid}}(\mathfrak{h}) + \phi_{\text{frac}}(\dot{d}, \nabla\dot{d}) + \phi_{\text{plast}}(\dot{\boldsymbol{\varepsilon}}^p, \dot{\alpha}, \dot{m}^p). \quad (27)$$

Dissipation-potential density for fluid flow. We follow Miehe et al. [2015b] and employ a dissipation-potential density in terms of the fluid flux \mathfrak{h} given by

$$\phi_{\text{fluid}}(\mathfrak{h}) = \frac{1}{2}\mathbf{K}^{-1} : (\mathfrak{h} \otimes \mathfrak{h}) \quad (28)$$

The permeability tensor \mathbf{K} at a given state $\{\boldsymbol{\varepsilon}, d, \nabla d\}$ is defined as

$$\mathbf{K}(\boldsymbol{\varepsilon}, d, \nabla d) = [1 - f(d)]\mathbf{K}_0 + f(d)\mathbf{K}_{\text{frac}}(\boldsymbol{\varepsilon}, \nabla d), \quad (29)$$

where \mathbf{K}_0 is the permeability tensor of the undamaged bulk and \mathbf{K}_{frac} is the permeability tensor within a crack. Clearly, the function $f(d)$ acts as an interpolation function between intact and fully damaged states of the material. In what follows, we select $f(d) = d^\epsilon$, where ϵ is an interpolation parameter.

While the permeability tensor of the undamaged bulk can be formulated in an isotropic manner based on the spatial permeability K as $\mathbf{K}_0 = \rho_f^2 K \mathbf{1}$, the permeability tensor within a crack can be expressed in terms of the fracture-opening function $w(\boldsymbol{\varepsilon}, \nabla d)$

$$\mathbf{K}_{\text{frac}}(\boldsymbol{\varepsilon}, \nabla d) = \rho_f^2 \frac{w^2(\boldsymbol{\varepsilon}, \nabla d)}{12\eta_f} (\mathbf{1} - \mathbf{n} \otimes \mathbf{n}) \quad \text{with} \quad \mathbf{n} := \frac{\nabla d}{|\nabla d|}, \quad (30)$$

which is anisotropic in nature. In the above definition, η_f is the fluid's dynamic viscosity. Note that the representation of the permeability in (30) is derived based on the lubrica-

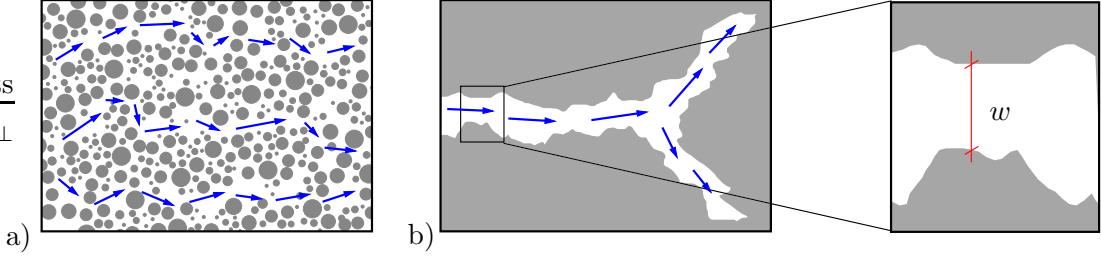


Figure 2: Schematic representation of a) fluid flow in porous medium according to Dracy’s law and b) within developing fractures according to Poiseuille–type law with fracture opening w .

tion theory and relates to Poiseuille-type flow within the fractures. In this context, the fracture-opening function is given as

$$w(\boldsymbol{\varepsilon}, \nabla d) = (\mathbf{n} \cdot \boldsymbol{\varepsilon} \cdot \mathbf{n}) L_{\perp}, \quad (31)$$

where L_{\perp} is the length of a line element that is perpendicular to the crack. In a finite-element representation this can be identified as the element size h^e .

Dissipation-potential density for fracture evolution. The dissipation-potential density associated with fracturing accounts for the dissipation of an evolving crack surface. It preserves thermodynamical consistency by ensuring a local irreversibility condition of the fracture phase field $\dot{d} \geq 0$, which can be achieved by introducing the indicator function $I(\dot{d})$.

For general Griffith-type fracturing the dissipation-potential density reads

$$\phi_{\text{frac}}^{g_c}(\dot{d}, \nabla d) := \frac{d}{dt} \left\{ g_c \gamma(d, \nabla d) \right\} + I(\dot{d}), \quad (32)$$

where g_c is Griffith’s critical energy-release rate. The indicator function $I(\dot{d})$ is given as

$$I(\dot{d}) := \begin{cases} 0 & \text{for } \dot{d} \geq 0, \\ \infty & \text{otherwise.} \end{cases} \quad (33)$$

Note that the fracture evolution described by (32) does not include any threshold value for the fracture evolution. In that case, damage occurs already at very small load levels. Hence, to clearly separate the material response during loading in elastic and plastic behavior as well as subsequent fracturing, the following dissipation-potential density will be used

$$\phi_{\text{frac}}(\dot{d}, \nabla d) := \frac{d}{dt} \left\{ [1 - g(d)] \psi_c + 2\psi_c l \gamma(d, \nabla d) \right\} + I(\dot{d}), \quad (34)$$

where ψ_c is a threshold value.

Dissipation-potential density for plastic response. The dissipation-potential density accounting for plastic behavior can be derived based on the principle of maximum dissipation. For that, the thermodynamical driving forces for the plastic strain, the hardening and the change of plastic fluid content need to be specified. Using the second law of thermodynamics (Clausius–Planck inequality) yields the driving forces as thermodynamical duals of $\boldsymbol{\varepsilon}^p$, α and m^p as

$$\begin{aligned}\boldsymbol{\sigma} &:= -\partial_{\boldsymbol{\varepsilon}^p}\psi = -\partial_{\boldsymbol{\varepsilon}^p}\psi_{\text{eff}} - \partial_{\boldsymbol{\varepsilon}^p}\psi_{\text{fluid}} = \boldsymbol{\sigma}_{\text{eff}} - b\rho_f\mu\mathbf{1} \\ \beta &:= -\partial_{\alpha}\psi = -\partial_{\alpha}\psi_{\text{plast}} \\ \mu &:= -\partial_{m^p}\psi = -\partial_{m^p}\psi_{\text{fluid}}.\end{aligned}\tag{35}$$

We denote the set of driving forces as $\mathfrak{F} = \{\boldsymbol{\sigma}, \beta, \mu\}$, wherein $\boldsymbol{\sigma}$ is the Cauchy stress, β is the hardening function and μ is the fluid potential. Based on that, we construct the dissipation-potential density ϕ_{plast} , which is formulated in terms of the constrained optimization problem

$$\phi_{\text{plast}}(\dot{\boldsymbol{\varepsilon}}^p, \dot{\alpha}, \dot{m}^p) := \sup_{\mathfrak{F} \in \mathbb{E}} [\boldsymbol{\sigma} : \dot{\boldsymbol{\varepsilon}}^p + \beta\dot{\alpha} + \mu\dot{m}^p].\tag{36}$$

In the above definition, the plastic driving forces are constrained to lie within the elastic domain $\mathbb{E} := \{\mathfrak{F} | f^p(\mathfrak{F}) \leq 0\}$, which is characterized by the yield function f^p . The latter will be specified at a later stage. By introducing the Lagrange multiplier λ^p the constrained optimization in (36) can be rewritten as

$$\phi_{\text{plast}}(\dot{\boldsymbol{\varepsilon}}^p, \dot{\alpha}, \dot{m}^p) := \sup_{\mathfrak{F}} \inf_{\lambda^p \geq 0} [\boldsymbol{\sigma} : \dot{\boldsymbol{\varepsilon}}^p + \beta\dot{\alpha} + \mu\dot{m}^p - \lambda^p f^p(\mathfrak{F})],\tag{37}$$

The latter representations are related to the rate-independent elastic-plastic material response, which leads to non-smooth evolution of plastic deformations. The non-smoothness can be relaxed by introducing viscous regularization, which yields the modified dissipation-potential density

$$\phi_{\text{plast}}(\dot{\boldsymbol{\varepsilon}}^p, \dot{\alpha}, \dot{m}^p) := \sup_{\mathfrak{F}} \underbrace{\left[\boldsymbol{\sigma} : \dot{\boldsymbol{\varepsilon}}^p + \beta\dot{\alpha} + \mu\dot{m}^p - \frac{1}{2\eta_p} \langle f^p(\mathfrak{F}) \rangle_+^2 \right]}_{\mathfrak{D}_{\text{plast}}}.\tag{38}$$

From a mathematical point of view this density is obtained from an optimization procedure with side condition, the latter of which is enforced by a quadratic penalty term. The penalty parameter is given by the plastic viscosity η_p .

In the present work it is assumed that the yield function f_{solid}^p describes the plastic response of the drained solid matrix. It is thus expressed in terms of the effective stresses $\boldsymbol{\sigma}_{\text{eff}}$ and the hardening function β . It should be equal to the yield function f^p of the

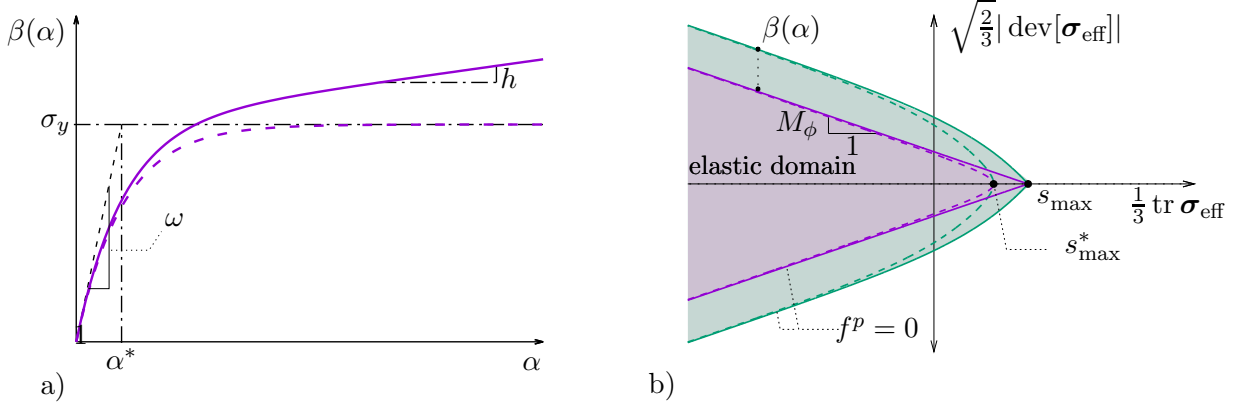


Figure 3: Hardening function $\beta(\alpha; d = 0)$ with linear hardening $h \neq 0$ (solid line) and without linear hardening $h = 0$ (dashed line), where $\alpha^* = (\frac{h}{\sigma_y} + \omega)^{-1}$ in a). In b) the yield function in two-dimensional hydrostatic-deviatoric plane with and without regularization (dashed/solid lines) where $s_{\max}^* = s_{\max} - \sqrt{\frac{2}{3}}q_1$. In green with hardening and no hardening in purple.

undrained bulk, which can be expressed in terms of the total stress $\boldsymbol{\sigma}$, the hardening function β and the fluid potential μ

$$f_{\text{solid}}^p(\boldsymbol{\sigma}_{\text{eff}}, \beta) = f^p(\boldsymbol{\sigma}, \beta, \mu). \quad (39)$$

A similar assumption has been made in [Armero \[1999\]](#). The starting point for the derivation of an appropriate yield function for the presented model is given by the yield function for frictional materials presented in [Kienle et al. \[2019\]](#), see also [Vermeer and de Borst \[1984\]](#) and [Lambrecht and Mieke \[2001\]](#). Making use of equations (35)₁ and (39) yields

$$f^p(\boldsymbol{\sigma}, \beta, \mu) = \sqrt{\frac{3}{2}} \sqrt{|\text{dev}[\boldsymbol{\sigma}]|^2 + M_\phi^2 q_1^2} - M_\phi (s_{\max} - \frac{1}{3} \text{tr} \boldsymbol{\sigma} - b \rho_f \mu) + \beta M_h(\boldsymbol{\sigma}, \mu), \quad (40)$$

where M_ϕ is related to the friction angle, q_1 is a parameter related to the regularization of the tip of the yield surface and s_{\max} is related to the cohesion of the material. The hardening response is limited to friction hardening by choosing the material function $M_h(\boldsymbol{\sigma}, \mu)$ as

$$M_h(\boldsymbol{\sigma}, \mu) = 1 - \sqrt{\frac{3}{2}} q_1 \exp \left[\frac{1}{3} \text{tr} \boldsymbol{\sigma} + b \rho_f \mu - s_{\max} \right]. \quad (41)$$

By inserting equation (35)₁ in equation (40) the yield function $f_{\text{solid}}^p(\boldsymbol{\sigma}_{\text{eff}}, \beta)$ can be recovered. The yield function in terms of the effective stress $\boldsymbol{\sigma}_{\text{eff}}$ is visualized in [Figure 3](#).

3.1.3 Potential of external loading

The external loading in form of mechanical tractions and fluid potential is formulated as

$$P_{\text{ext}}(\dot{\mathbf{U}}) = \int_{\partial\mathcal{B}_t} \bar{\mathbf{t}} \cdot \dot{\mathbf{u}} \, dA - \int_{\partial\mathcal{B}_\mu} \bar{\mu} \mathbf{h} \cdot \mathbf{n} \, dA, \quad (42)$$

where $\bar{\mathbf{t}}$ is the mechanical traction vector applied on the traction boundary $\partial\mathcal{B}_t$ of the domain \mathcal{B} . The fluid contribution is due to the fluid transport over the boundary $\partial\mathcal{B}_\mu$ of the domain \mathcal{B} , where the fluid potential $\bar{\mu}$ is applied.

3.2 Minimization principle and mixed variational principle

Based on the above introduced functions we can introduce a rate-type minimization principle that governs the boundary-value problems of porous-elastic-plastic solids at fracture

$$\dot{\mathbf{U}}^* = \arg \left\{ \inf_{\dot{\mathbf{U}} \in \mathfrak{W}} \Pi(\dot{\mathbf{U}}; \mathbf{U}) \right\} \quad (43)$$

where $\mathfrak{W} = \{\mathcal{W}_{\dot{\mathbf{u}}}, \mathcal{W}_{\mathbf{h}}, \mathcal{W}_{\dot{d}}, \mathcal{W}_{\dot{\boldsymbol{\varepsilon}}^p}, \mathcal{W}_{\dot{\alpha}}, \mathcal{W}_{\dot{m}^p}\}$ is the set of admissible spaces corresponding to the set of the rate of unknowns $\dot{\mathbf{U}}$. The admissible spaces are given as

$$\begin{aligned} \mathcal{W}_{\dot{\mathbf{u}}} &:= \{\dot{\mathbf{u}} \in H^1(\mathcal{B}) \mid \dot{\mathbf{u}} = \dot{\bar{\mathbf{u}}} \text{ on } \partial\mathcal{B}_u\}, & \mathcal{W}_{\mathbf{h}} &:= \{\mathbf{h} \in H(\text{div}, \mathcal{B}) \mid \mathbf{h} \cdot \mathbf{n} = \bar{h} \text{ on } \partial\mathcal{B}_h\} \\ \mathcal{W}_{\dot{d}} &:= \{\dot{d} \in H^1(\mathcal{B})\}, & \mathcal{W}_{\dot{\boldsymbol{\varepsilon}}^p} &:= \{\dot{\boldsymbol{\varepsilon}}^p \in L^2\} \\ \mathcal{W}_{\dot{\alpha}} &:= \{\dot{\alpha} \in L^2\}, & \mathcal{W}_{\dot{m}^p} &:= \{\dot{m}^p \in L^2\}. \end{aligned} \quad (44)$$

Combining the global minimization principle (43) with the local maximization principle in (38) yields the mixed variational principle

$$\{\dot{\mathbf{U}}^*, \mathfrak{F}^*\} = \arg \left\{ \inf_{\dot{\mathbf{U}} \in \mathfrak{W}} \sup_{\mathfrak{F} \in L^2} \int_{\mathcal{B}} \pi^*(\dot{\mathbf{c}}, \mathfrak{F}; \mathbf{c}) \, dV - P_{\text{ext}}(\dot{\mathbf{U}}) \right\} \quad (45)$$

where $\pi^*(\dot{\mathbf{c}}, \mathfrak{F}; \mathbf{c})$ is the mixed potential density. It reads

$$\pi^*(\dot{\mathbf{c}}, \mathfrak{F}; \mathbf{c}) = \frac{d}{dt} \psi(\mathbf{c}) + \mathfrak{D}_{\text{plast}}(\dot{\boldsymbol{\varepsilon}}^p, \dot{\alpha}, \dot{m}^p, \mathfrak{F}) + \phi_{\text{fluid}}(\mathbf{h}) + \phi_{\text{frac}}(\dot{d}, \nabla \dot{d}). \quad (46)$$

Performing the variation of (46) at a fixed state \mathbf{c} , we obtain the Euler equations of the

mixed variational principle (45) for the global unknowns as

$$\begin{aligned}
 \operatorname{div}[\partial_\varepsilon\psi] &= \mathbf{0} && \text{in } \mathcal{B} \\
 \nabla[\partial_m\psi] + \partial_{\mathfrak{h}}\phi &= \mathbf{0} && \text{in } \mathcal{B} \\
 \partial_d\psi + \partial_d\phi - \operatorname{div}[\partial_{\nabla d}\phi] &\ni 0 && \text{in } \mathcal{B} \\
 -\partial_m\psi + \bar{\mu} &= 0 && \text{on } \partial\mathcal{B}_\mu \\
 \partial_\varepsilon\psi \cdot \mathbf{n} - \bar{\mathbf{t}} &= \mathbf{0} && \text{on } \partial\mathcal{B}_t \\
 \partial_{\nabla d}\phi \cdot \mathbf{n} &= 0 && \text{on } \partial\mathcal{B}_t
 \end{aligned} \tag{47}$$

and the local unknowns with the corresponding thermodynamic duals as

$$\begin{aligned}
 \partial_{\varepsilon^p}\psi + \boldsymbol{\sigma} &= \mathbf{0} && \text{in } \mathcal{B} \\
 \partial_\alpha\psi + \beta &= 0 && \text{in } \mathcal{B} \\
 \partial_{m^p}\psi + \mu &= 0 && \text{in } \mathcal{B} \\
 \dot{\varepsilon}^p - \lambda_v^p \partial_\sigma f^p &= \mathbf{0} && \text{in } \mathcal{B} \\
 \dot{\alpha} - \lambda_v^p \partial_\beta f^p &= 0 && \text{in } \mathcal{B} \\
 \dot{m}^p - \lambda_v^p \partial_\mu f^p &= 0 && \text{in } \mathcal{B}
 \end{aligned} \tag{48}$$

The equations in (47) represent the global balance laws and the corresponding Neumann boundary conditions. In (48) the definition of the thermodynamic duals of the local fields as well as their evolution equations are given. In the latter, we introduced the visco-plastic multiplier $\lambda_v^p := \frac{1}{\eta_p} \langle f^p \rangle_+$.

Condensation of local variables. The set of the rate of the primary fields can be split into a local and global part. The former is given as $\dot{\mathbf{U}}_l = \{\dot{\varepsilon}^p, \dot{\alpha}, \dot{m}^p\}$ and the latter arises as $\dot{\mathbf{U}}_g = \dot{\mathbf{U}} \setminus \dot{\mathbf{U}}_l = \{\dot{\mathbf{u}}, \dot{d}, \dot{\mathfrak{h}}\}$. The set of the rate of the local fields $\dot{\mathbf{U}}_l$ is governed by the mixed variational principle

$$\{\dot{\mathbf{U}}_l^*, \mathfrak{F}^*\} = \arg \left\{ \inf_{\dot{\mathbf{U}}_l} \sup_{\mathfrak{F}} \pi^*(\dot{\mathbf{e}}, \mathfrak{F}; \mathbf{e}) \right\} \tag{49}$$

In order to obtain a solution for $\dot{\mathbf{U}}_g$ the reduced potential density is introduced as

$$\pi_{\text{red}}^*(\dot{\mathbf{e}}_{\text{red}}; \mathbf{e}_{\text{red}}) = \inf_{\dot{\mathbf{U}}_l} \sup_{\mathfrak{F}} \pi^*(\dot{\mathbf{e}}, \mathfrak{F}; \mathbf{e}), \tag{50}$$

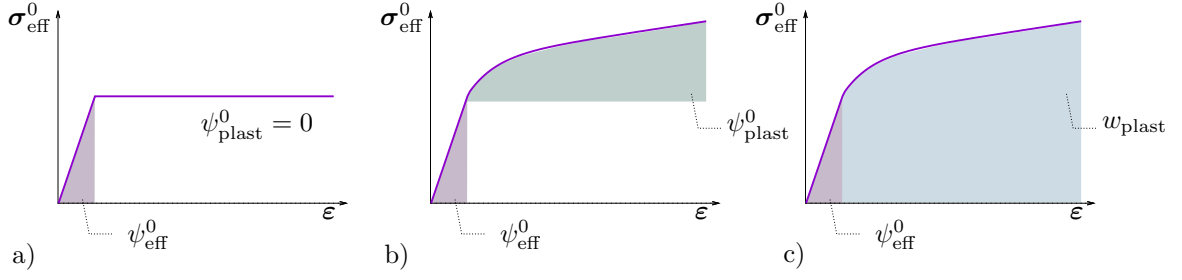


Figure 4: Visualization of the different energy contributions to the crack driving history field \mathcal{H} . For the representation of \mathcal{H} in (53)₂ only the elastic energy and the energy arising from the hardening, as show in a) and b), will drive the crack. For ideal plasticity the plastic energy vanishes ($\psi_{\text{plast}}^0 = 0$) leading to pure brittle fracture, see a). By using (56) the crack is driven by the elastic energy and the full plastic work, see c).

where the reduced constitutive state $\mathbf{c}_{\text{red}} = \{\boldsymbol{\varepsilon}, m, d, \nabla d\}$ and its evolution $\dot{\mathbf{c}}_{\text{red}} = \{\dot{\boldsymbol{\varepsilon}}, \dot{\mathbf{h}}, \text{div } \dot{\mathbf{h}}, \dot{d}, \nabla \dot{d}\}$ are introduced. The set of the rate of the global fields is given by the following minimization principle

$$\dot{\boldsymbol{\mathcal{U}}}_{\text{g}}^* = \{\dot{\mathbf{u}}^*, \dot{d}^*, \dot{\mathbf{h}}^*\} = \arg \left\{ \inf_{\dot{\mathbf{u}} \in \mathcal{W}_{\dot{\mathbf{u}}}} \inf_{\dot{d} \in \mathcal{W}_{\dot{d}}} \inf_{\dot{\mathbf{h}} \in \mathcal{W}_{\dot{\mathbf{h}}}} \int_{\mathcal{B}} \pi_{\text{red}}^*(\dot{\mathbf{c}}_{\text{red}}; \mathbf{c}_{\text{red}}) \, dV - P_{\text{ext}}(\dot{\boldsymbol{\mathcal{U}}}) \right\} \quad (51)$$

3.3 Modification of the fracture driving force

In this section a closer look at equation (47)₃ is taken. Inserting the definitions of the energy density and the dissipation potential density yields

$$-2(1-d)[\psi_{\text{eff}}^0 + \psi_{\text{plast}}^0 - \psi_c] + 2\psi_c(d - l^2 \Delta d) + \partial_j I \ni 0. \quad (52)$$

By introducing the crack driving history field \mathcal{H} this is modified to

$$-2(1-d)\mathcal{H} + 2\psi_c(d - l^2 \Delta d) = 0 \quad \text{with} \quad \mathcal{H} := \max_{s \in [0, t]} \langle \psi_{\text{eff}}^0 + \psi_{\text{plast}}^0 - \psi_c \rangle_+. \quad (53)$$

This follows the notation for brittle fracture in Miehe et al. [2010a] and for ductile fracture in Miehe et al. [2015a, 2016a].

For plasticity models with a yield limit that is independent of the stress state it is possible to formulate a plastic energy density $\tilde{\psi}_{\text{plast}}^0(\alpha)$, which contains not only the work of the hardening for the solid matrix but also the work of the ideal plastic deformation of the solid matrix. One such example is given by von-Mises plasticity, for which we can

write

$$\tilde{\psi}_{\text{plast}}^0(\alpha) \stackrel{\text{von Mises}}{=} w_{\text{plast}} \quad \text{with} \quad w_{\text{plast}} \stackrel{(49)}{=} \int \boldsymbol{\sigma}_{\text{eff}}^0 : \dot{\boldsymbol{\epsilon}}^p \, dt \quad (54)$$

Note that the undamaged effective stress $\boldsymbol{\sigma}_{\text{eff}}^0$ acting on the solid matrix is used here. The plastic work w_{plast} can alternatively be expressed in terms of the undamaged total stress $\boldsymbol{\sigma}^0$ and the fluid potential μ as

$$w_{\text{plast}} = \int \boldsymbol{\sigma}_{\text{eff}}^0 : \dot{\boldsymbol{\epsilon}}^p \, dt = \int \boldsymbol{\sigma}^0 : \dot{\boldsymbol{\epsilon}}^p + \mu \dot{m}^p \, dt. \quad (55)$$

Since the construction of an energy density $\tilde{\psi}_{\text{plast}}^0$ like (54)₁ is not possible for more complicated plasticity models such as the Drucker–Prager model, the crack driving history field in (53)₂ is modified to

$$\mathcal{H} = \max_{s \in [0, t]} \langle \psi_{\text{eff}}^0 + w_{\text{plast}} - \psi_c \rangle_+. \quad (56)$$

With the representation of the crack driving history field in (56) it is possible to model ductile fracture evolution that is driven by the elastic and the ideal plastic deformation as well as the hardening. With the representation in (53)₂ and the definition of the plastic energy in (24)₂ it is only possible to model a ductile fracture evolution which is driven by the elastic deformation and the hardening.

3.3.1 Relation between plastic strain and change of fluid content

Based on the construction of the yield function, see (39), the evolution of the plastic strain (48)₄ can be reformulated as

$$\dot{\boldsymbol{\epsilon}}^p = \lambda_v^p \partial_{\boldsymbol{\sigma}} f^p = \lambda_v^p \partial_{\boldsymbol{\sigma}_{\text{eff}}} f_{\text{solid}}^p. \quad (57)$$

Furthermore, reformulation of the evolution of the change of plastic fluid content (48)₆ yields

$$\dot{m}^p = \lambda_v^p \partial_{\mu} f^p = \lambda_v^p \rho_f b \, \text{tr}(\partial_{\boldsymbol{\sigma}_{\text{eff}}} f_{\text{solid}}^p). \quad (58)$$

Combining the above two equations gives a relation between the evolution of the plastic strain and the evolution of the change of the plastic fluid content

$$\dot{m}^p = \rho_f b \, \text{tr} \dot{\boldsymbol{\epsilon}}^p. \quad (59)$$

We observe that the change of the plastic fluid content depends exclusively on volumetric plastic deformation.

4 Numerical Treatment

4.1 Incremental variational formulation

The incremental version of the rate-type potential introduced in Section 3 is obtained by algorithmic time integration over a given time step $\tau = [t_n, t_{n+1})$. For a pure Dirichlet problem ($P_{\text{ext}} = 0$) we arrive at

$$\Pi^\tau(\mathbf{u}, \mathfrak{F}) = \text{Algo} \left\{ \int_{t_n}^{t_{n+1}} \Pi(\dot{\mathbf{u}}, \mathfrak{F}; \mathbf{e}) dt \right\} = \int_B \pi^{*\tau}(\mathbf{e}, \mathfrak{F}; \mathbf{e}_n) dV, \quad (60)$$

where $\pi^{*\tau}(\mathbf{e}, \mathfrak{F}; \mathbf{e}_n)$ is the incremental potential density. It is given in terms of the energy density ψ , the incremental fluid and fracture dissipation-potential density ϕ_{fluid}^τ and ϕ_{frac}^τ , respectively, as well as the incremental dissipation density related to the visco-plastic behavior $\mathfrak{D}_{\text{plast}}^\tau$ as

$$\pi^{*\tau}(\mathbf{e}, \mathfrak{F}; \mathbf{e}_n) = \psi(\mathbf{e}) + \mathfrak{D}_{\text{plast}}^\tau(\boldsymbol{\varepsilon}^p, \alpha, m^p, \mathfrak{F}; \boldsymbol{\varepsilon}_n^p, \alpha_n, m_n^p) + \phi_{\text{fluid}}^\tau(\mathfrak{h}) + \phi_{\text{frac}}^\tau(d, \nabla d, d_n). \quad (61)$$

The individual dissipative contributions read

$$\begin{aligned} \phi_{\text{fluid}}^\tau &= \tau \phi_{\text{fluid}}(\mathfrak{h}) \\ \phi_{\text{frac}}^\tau &= [1 - g(d)]\psi_c + 2\psi_c l \gamma(d, \nabla d) + I^\tau(d, d_n) \\ \mathfrak{D}_{\text{plast}}^\tau &= \boldsymbol{\sigma} : (\boldsymbol{\varepsilon}^p - \boldsymbol{\varepsilon}_n^p) + \beta(\alpha - \alpha_n) + \mu(m^p - m_n^p) + \frac{\tau}{2\eta_p} \langle f^p(\mathfrak{F}) \rangle_+^2. \end{aligned} \quad (62)$$

Furthermore the fluid mass balance (6)₂ is satisfied by the implicit update

$$m = m_n - \tau \operatorname{div} \mathfrak{h}. \quad (63)$$

Condensation of local variables. Similar as in the continuous problem, the set of primary fields can be decomposed into a local and global part. Again, the local fields are identified as $\mathbf{u}_1 = \{\boldsymbol{\varepsilon}^p, \alpha, m^p\}$ and the global fields as $\mathbf{u}_g = \mathbf{u} \setminus \mathbf{u}_1 = \{\mathbf{u}, d, \mathfrak{h}\}$. The local fields are governed by the mixed variational principle

$$\boxed{\mathbf{u}_1^* = \arg \left\{ \inf_{\mathbf{u}_1} \sup_{\mathfrak{F}} \pi^{*\tau}(\mathbf{e}, \mathfrak{F}; \mathbf{e}_n) \right\}} \quad (64)$$

Using the representation (38) the mixed variational principle (64) leads to the following condition

$$\partial_{\mathbf{u}_1, \mathfrak{F}} \pi^* = \begin{bmatrix} \partial_{\boldsymbol{\varepsilon}^p} \psi + \boldsymbol{\sigma} \\ \partial_{\alpha} \psi + \beta \\ \partial_{m^p} \psi + \mu \\ \boldsymbol{\varepsilon}^p - \boldsymbol{\varepsilon}_n^p - \gamma_v^p \partial_{\boldsymbol{\sigma}} f^p \\ \alpha - \alpha_n - \gamma_v^p \partial_{\beta} f^p \\ m^p - m_n^p - \gamma_v^p \partial_{\mu} f^p \end{bmatrix} = \mathbf{0}. \quad (65)$$

Here, $\gamma_v^p := \tau \lambda_v^p = \frac{\tau}{\eta_p} \langle f^p \rangle_+$ is the incremental visco-plastic multiplier. The local system of equations in (65) is solved via a general return mapping scheme summarized in Box 1.

0. Get trial values $[\boldsymbol{\varepsilon}^{e,\text{tr}}; m^{e,\text{tr}}; \alpha^{\text{tr}}]^T = [(\boldsymbol{\varepsilon} - \boldsymbol{\varepsilon}_n^p); (m - m_n^p); \alpha_n]^T$

1. Set initial values $[\boldsymbol{\varepsilon}^e; m^e; \alpha]^T = [\boldsymbol{\varepsilon}^{e,\text{tr}}; m^{e,\text{tr}}; \alpha^{\text{tr}}]$ and $\gamma_v^p = 0$.

2. Compute derivatives of energy density and yield function

$$\begin{array}{l} \psi(\boldsymbol{\varepsilon}^e, m^e, \alpha; d) \quad \mathbf{s} = \begin{bmatrix} \psi_{,\boldsymbol{\varepsilon}^e} \\ \psi_{,m^e} \\ \psi_{,\alpha} \end{bmatrix} \quad \mathbb{E} = \begin{bmatrix} \psi_{,\boldsymbol{\varepsilon}^e \boldsymbol{\varepsilon}^e} & \psi_{,\boldsymbol{\varepsilon}^e m^e} & \psi_{,\boldsymbol{\varepsilon}^e \alpha} \\ \psi_{,m^e \boldsymbol{\varepsilon}^e} & \psi_{,m^e m^e} & \psi_{,m^e \alpha} \\ \psi_{,\alpha \boldsymbol{\varepsilon}^e} & \psi_{,\alpha m^e} & \psi_{,\alpha \alpha} \end{bmatrix} \\ f^p(\boldsymbol{\sigma}, \mu, \beta) \quad \mathbf{n} = \begin{bmatrix} f^p_{,\boldsymbol{\sigma}} \\ f^p_{,\mu} \\ f^p_{,\beta} \end{bmatrix} \quad \mathbb{F} = \begin{bmatrix} f^p_{,\boldsymbol{\sigma} \boldsymbol{\sigma}} & f^p_{,\boldsymbol{\sigma} \mu} & f^p_{,\boldsymbol{\sigma} \beta} \\ f^p_{,\mu \boldsymbol{\sigma}} & f^p_{,\mu \mu} & f^p_{,\mu \beta} \\ f^p_{,\beta \boldsymbol{\sigma}} & f^p_{,\beta \mu} & f^p_{,\beta \beta} \end{bmatrix} \end{array}$$

3. Check for yielding. If yielding do a local Newton iteration

if $f^p < 0$ **then** // elastic step

 | set $[\boldsymbol{\sigma}; \psi_{,m}]^T = [\psi_{,\boldsymbol{\varepsilon}^e}; \psi_{,m^e}]^T$ and $\mathbb{E}^{\text{ep}} = \mathbb{E}$

 | **return**

else // plastic step

 | **compute** residual vector

 | $\mathbf{r} := [(\boldsymbol{\varepsilon}_n^p - \boldsymbol{\varepsilon}^p); (m_n^p - m^p); (\alpha_n - \alpha)]^T + \gamma_v^p \mathbf{n}$

 | **check** if local Newton is converged

 | **if** $[\sqrt{\mathbf{r}^T \mathbf{r} + [f^p - \frac{\eta_p}{\tau} \gamma_v^p]^2} < \text{tol}]$ go to 4.

 | **compute** incremental plastic parameter

 | $\Delta \gamma_v^p = \frac{1}{C} [f^p - \mathbf{n}^T \mathbb{X} \mathbf{r}]$ with $C := \mathbf{n}^T \mathbb{X} \mathbf{n} + \frac{\eta_p}{\tau}$ and $\mathbb{X} := [\mathbb{E}^{-1} + \gamma_v^p \mathbb{F}]^{-1}$

 | **compute** incremental strains, plastic fluid content and hardening variable

 | $[\Delta \boldsymbol{\varepsilon}^p; \Delta m^p; \Delta \alpha]^T = -\mathbb{E}^{-1} \mathbb{X} [\mathbf{r} + \Delta \gamma_v^p \mathbf{n}]$

 | **update** plastic quantities

 | $[\boldsymbol{\varepsilon}^p; m^p; \alpha; \gamma_v^p]^T \leftarrow [\boldsymbol{\varepsilon}^p; m^p; \alpha; \gamma_v^p]^T + [\Delta \boldsymbol{\varepsilon}^p; \Delta m^p; \Delta \alpha; \Delta \gamma_v^p]^T$

 | **update** elastic quantities

 | $[\boldsymbol{\varepsilon}^e; m^e]^T = [(\boldsymbol{\varepsilon} - \boldsymbol{\varepsilon}^p); (m - m^p)]^T$

 | go to 2.

4. For plastic step: Obtain stresses and consistent moduli

$$[\boldsymbol{\sigma}; \psi_{,m}]^T = [\psi_{,\boldsymbol{\varepsilon}^e}; \psi_{,m^e}]^T \quad \text{and} \quad \mathbb{E}^{\text{ep}} = \mathbb{X} - \frac{1}{C} [\mathbb{X} \cdot \mathbf{n}] \otimes [\mathbf{n} \cdot \mathbb{X}]$$

Box 1: Return mapping and tangent moduli for poro-elasto-plasticity. It is based on the algorithm for elasto-plasticity in Miehe [1998].

Reduced global problem. In order to obtain a solution for \mathbf{u}_g the reduced potential density is introduced

$$\pi_{\text{red}}^{*\tau}(\mathbf{c}_{\text{red}}) = \inf_{\mathbf{u}_1} \sup_{\mathfrak{F}} \pi^{*\tau}(\mathbf{c}, \mathfrak{F}; \mathbf{c}_n), \quad (66)$$

where the reduced constitutive state $\mathbf{c}_{\text{red}} = \{\boldsymbol{\varepsilon}, \mathfrak{h}, \text{div } \mathfrak{h}, d, \nabla d\}$ is introduced. The global fields are then given by the minimization principle

$$\mathbf{u}_g^* = \{\mathbf{u}^*, d^*, \mathfrak{h}^*\} = \arg \left\{ \inf_{\mathbf{u} \in \mathcal{W}_u} \inf_{d \in \mathcal{W}_d} \inf_{\mathfrak{h} \in \mathcal{W}_h} \int_{\mathcal{B}} \pi_{\text{red}}^{*\tau}(\mathbf{c}_{\text{red}}) \, dV \right\}, \quad (67)$$

with the admissible spaces

$$\begin{aligned} \mathcal{W}_u &:= \{\mathbf{u} \in H^1(\mathcal{B}) \mid \mathbf{u} = \bar{\mathbf{u}} \text{ on } \partial\mathcal{B}_u\}, \\ \mathcal{W}_h &:= \{\mathfrak{h} \in H(\text{div}, \mathcal{B}) \mid \mathfrak{h} \cdot \mathbf{n} = \bar{h} \text{ on } \partial\mathcal{B}_h\}, \\ \mathcal{W}_d &:= \{d \in H^1(\mathcal{B})\}. \end{aligned} \quad (68)$$

4.2 Space-time-discrete finite-element formulation

Considering a finite-element discretization $\mathcal{T}^h(\mathcal{B})$, the discrete state vector \mathbf{d} containing the discrete values of $\{\mathbf{u}, \mathfrak{h}, d\}$ and the interpolation of the constitutive state $\mathbf{c}_{\text{red}}^h = \mathbf{B}\mathbf{d}$ the global minimization principle (67) can be written as

$$\mathbf{d}^* = \arg \{ \inf_{\mathbf{d}} \Pi^{\tau h}(\mathbf{d}) \} \quad \text{with} \quad \Pi^{\tau h}(\mathbf{d}) = \int_{\mathcal{B}} \pi_{\text{red}}^{*\tau h}(\mathbf{B}\mathbf{d}) \, dV. \quad (69)$$

Here, we employ the shape functions from [Raviart and Thomas \[1977\]](#) for the interpolation of the fluid flux, see also [Teichtmeister et al. \[2019\]](#). The nodal displacement is interpolated by the shape functions of the enhanced-assumed-strain formulation, see [Simo and Rifai \[1990\]](#). The interpolation of the nodal phase-field values is done by the standard Q_1 -type shape functions.

The global algebraic minimization principle (69) leads to the following condition

$$\mathbf{R} := \Pi_{,\mathbf{d}}^{\tau h} = \int_{\mathcal{B}} \mathbf{B}^T \mathbf{S} \, dV = \mathbf{0} \quad (70)$$

where the generalized array \mathbf{S} is introduced. This array is defined as follows

$$\mathbf{S} := \begin{bmatrix} \psi_{,\varepsilon^h} \\ -\tau\psi_{,m^h} \\ \tau\phi_{,\mathfrak{h}^h} \\ \hline -2(1-d)\mathcal{H} + \phi_{,d^h}^{\tau'} \\ \phi_{,\nabla d^h}^{\tau} \end{bmatrix} \quad (71)$$

Note that this array is not obtained by straightforward differentiation of (69)₂, i.e. we have in general $\mathbf{S} \neq \partial_{\mathbf{e}_{\text{red}}^h} \pi_{\text{red}}^{*\tau h}$. This is due to the consideration of the history field \mathcal{H} in (53). Above, we have introduced the $\phi^{\tau'} = \phi^{\tau} - I^{\tau}(d, d_n)$, where $I^{\tau}(d, d_n)$ is the time discrete version of the indicator function (33). The system of equations (70) is solved by a Newton–Raphson-type iteration yielding

$$\mathbf{d} \leftarrow \mathbf{d} - \mathbf{K}^{-1} \mathbf{R} \quad \text{with} \quad \mathbf{K} := \Pi_{,\mathbf{d}\mathbf{d}}^{\tau h} = \int_B \mathbf{B}^T \mathbf{C} \mathbf{B} \, dV. \quad (72)$$

The generalized tangent array \mathbf{C} is given as

$$\mathbf{C} := \partial_{\mathbf{e}_{\text{red}}^h} \mathbf{S} = \begin{bmatrix} \boxed{\begin{matrix} \mathbf{E}_{\varepsilon\varepsilon}^{\text{ep}} & -\tau\mathbf{E}_{\varepsilon m}^{\text{ep}} & 0 \\ -\tau\mathbf{E}_{m\varepsilon}^{\text{ep}} & \tau^2\mathbf{E}_{mm}^{\text{ep}} & 0 \\ 0 & 0 & \tau\phi_{,\mathfrak{h}^h\mathfrak{h}^h} \end{matrix}} & \cdot & \cdot \\ \cdot & \cdot & 0 \\ \cdot & \cdot & 0 \\ \cdot & \cdot & 0 & \boxed{\begin{matrix} 2\mathcal{H} + \phi_{,d^h}^{\tau'} & 0 \\ 0 & \phi_{,\nabla d^h}^{\tau} \end{matrix}} \end{bmatrix}. \quad (73)$$

Here "0" indicates that the corresponding derivative does not exist. The derivatives at the slots labeled with "." indeed exist but are not needed due to the modification of the fracture driving force (53) as consequence of an operator split. The latter leads to a decoupling of the related fields so that the two boxed sub-blocks in (73) can be treated in separate solution steps. The so called one-pass solution strategy is utilized here (Miehe et al. [2010a, 2015a]). This means that the displacement and flux is updated first and then the fracture phase-field is updated. This might underestimate the speed of the fracture evolution but can be controlled by the choice of an appropriated time step size τ (Kienle et al. [2019]).

Table 1: Material parameters for rigid footing test.

Lamé parameter	$\lambda = 180.0$	GN/m ²	slope yield function	$M_\phi = 0.6$	–
Lamé parameter	$G = 31.0$	GN/m ²	position of peak	$s_{\max} = 4.0$	MN/m ²
hardening modulus	$h = 0.035$	MN/m ²	Biot’s modulus	$M = 25.0$	GN/m ²
saturated yield shift	$\sigma_y = 0.1$	MN/m ²	Biot’s coefficient	$b = 0.5$	–
saturation parameter	$\omega = 2.0$	–	fluid dyn. viscosity	$\eta_f = 1.0 \cdot 10^{-3}$	Ns/m ²
plastic viscosity	$\eta_p = 5 \cdot 10^{-6}$	s	permeability	$K = 9.8 \cdot 10^{-12}$	m ³ s/kg
perturbation parameter	$q_1 = 0.04$	MN/m ²	fluid density	$\rho_f = 1000.0$	kg/m ³

5 Numerical Examples

In the following we present a sequence of numerical examples that demonstrate the capabilities of the model formulation. The examples start with a test of a porous-elastic-plastic medium that is surcharged with a rigid footing leading to the creation of shear bands. Furthermore, we analyze the effect of different driving forces on porous-elastic-plastic fracture evolution. The latter analysis is extended to the comparison of porous-elastic and porous-elastic-plastic materials response leading to the evolution of Hydraulically induced fractures.

5.1 Rigid-footing test on porous-elastic-plastic medium

In the first example we consider a rigid footing test without fracture evolution. Our goal is to analyze the effect of plasticity as well as fluid flux and storage on the system’s response. We thus take into account three different material types:

- i) drained elastic-plastic material,
- ii) undrained porous-elastic material,
- iii) undrained porous-elastic-plastic material with different permeabilities.

The drained elastic-plastic material is recovered by setting Biot’s modulus and coefficient to zero ($M = 0, b = 0$). In order to model the undrained porous-elastic material, the yield limit is increased to a very high value by setting $s_{\max} = 1 \cdot 10^4$ MN/m². For the undrained porous-elastic-plastic material all contributions of the model are active, hence no artificial choice of any material parameter is necessary. In order to analyze the effect of the permeability on the overall model response, we consider different magnitudes of permeabilities given by an original value K as well as a reduced and an increased permeability ($K/5$ and $5K$, respectively). The chosen material parameters are listed in Table 1.

The geometry and boundary conditions are shown in Figure 5. Due to the symmetry of loading and geometry only one half of the specimen is discretized by 2,376 quadri-

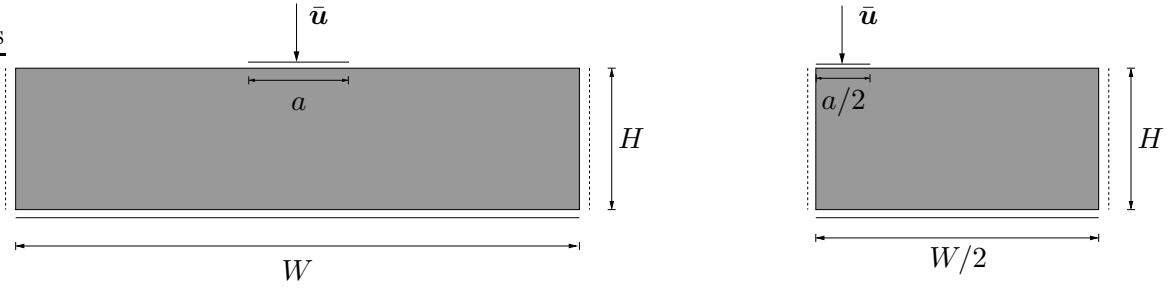


Figure 5: Rigid footing test: Geometry and boundary conditions. Bottom is mechanically fixed, left and right edge is mechanically fixed in horizontal direction. Bottom, left and right is impermeable.

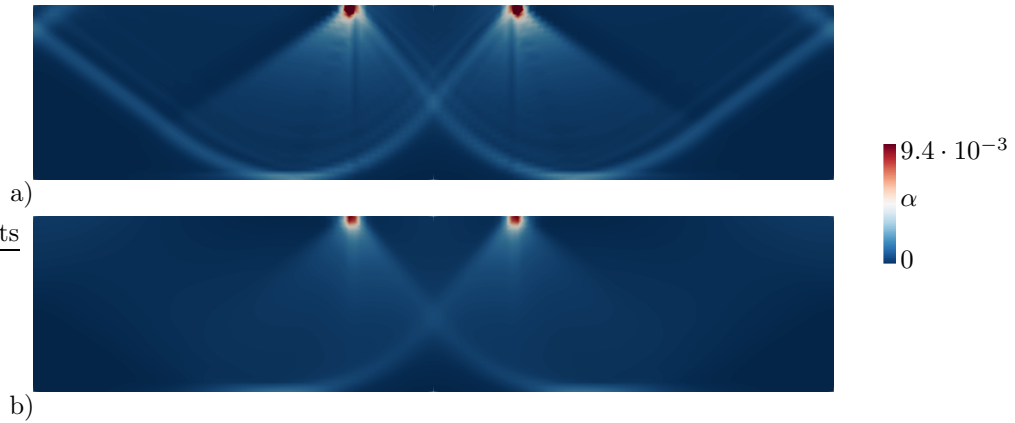


Figure 6: Rigid footing test: Distribution of the hardening variable α in drained elastic-plastic material in a) and undrained porous-elastic-plastic material in b).

lateral Raviart–Thomas-type enhanced-assumed-strain elements. The dimensions are $H = 4.758$ m, $W = 23.088$ m and $a = 4.587$ m. The loading increment is $\Delta \bar{u} = 5 \cdot 10^{-6}$ m. The loading is linearly increased until a total displacement of $\bar{u} = 0.0023$ m is reached.

In Figure 6 the distribution of the hardening variable α for the drained elastic-plastic material and undrained porous-elastic-plastic material is shown. It can be seen that the plastic deformation is more pronounced in the case of the drained material. This leads to the conclusion that the fluid within the material leads to an additional hardening effect. The load-displacement curve in Figure 7 also shows this behaviour. Furthermore, a lower permeability leads to more pronounced hardening. This can be explained by the fact that the transport of the fluid is hindered and thus requires more work, see Figure 7.

Next, the distribution of the change of elastic fluid content m^e in the domain for the undrained porous-elastic material is compared with the one of the undrained porous-elastic-plastic material, see Figure 8.

Note that for the elastic material the fluid is squeezed out right underneath the area where the loading is applied (see the negative change of the elastic fluid content at the boundary of the applied footing depicted in Figure 8a). Opposed to that, in case of the

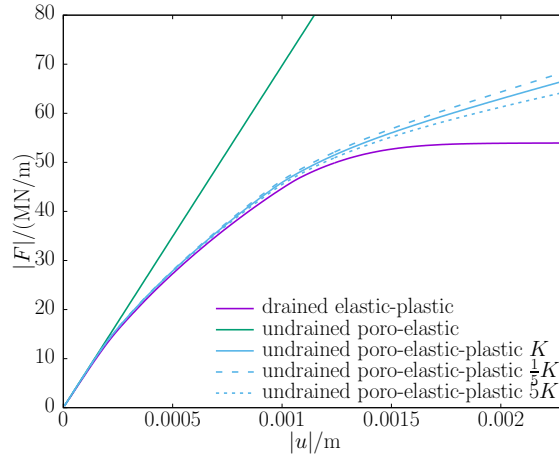


Figure 7: Rigid footing: Load displacement curve for the different tested material types. The load and displacement is taken from the area were the displacement is prescribed, see Figure 5.

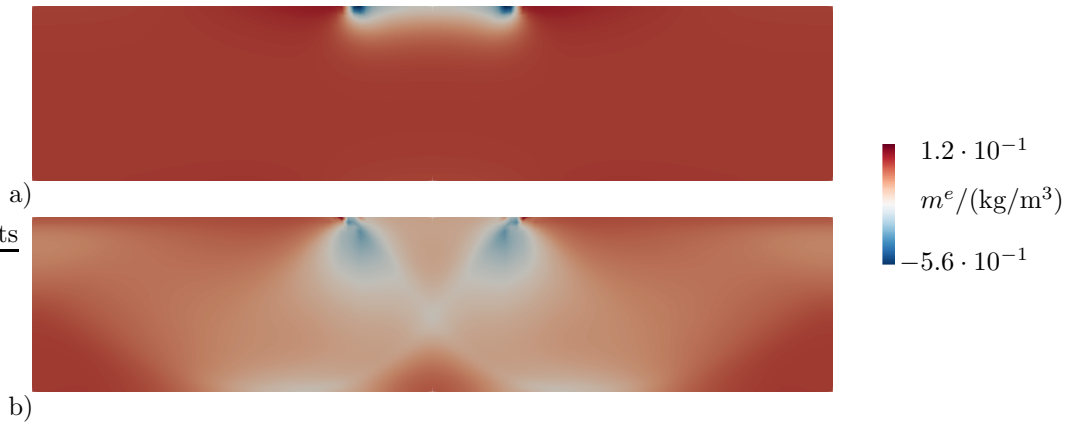


Figure 8: Rigid footing test. Change of the elastic fluid content m^e for undrained porous-elastic material in a) and in b) for undrained porous-elastic-plastic material.

elastic-plastic material, the highest (negative) change of elastic fluid content is occurring in a more diffuse region that also extends to the bulk (see Figure 8b). This is precisely the area where most of the plastic deformation is happening, as can be observed in Figure 6 b). This phenomenon can be explained by the fact that the plastic deformation leads to a positive change of the plastic fluid content. Due to the additive decomposition of the change of the fluid content and the fact that no fluid is injected, the change of the elastic fluid content becomes negative in the plastifying areas.

We depict the distribution of the change of the elastic m^e , the plastic m^p and total fluid content m for the undrained porous-elastic-plastic material in Figure 9. One can observe that the change of the total fluid content m is strongly dominated by the change of the plastic fluid content m^p .

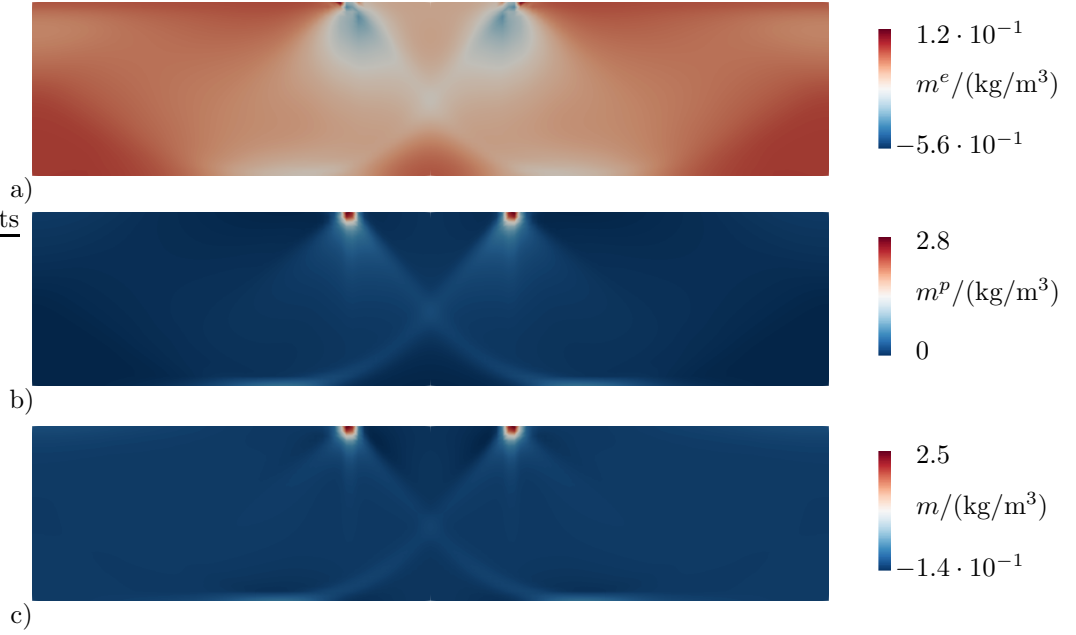


Figure 9: Rigid footing test: Change of fluid content for undrained porous-elastic-plastic material. Change of elastic fluid content m^e in a), change of plastic fluid content m^p in b) and change of total fluid content m in c).

Table 2: Material parameters for hydraulically induced fracture.

Lamé parameter	$\lambda = 180.0$	GN/m ²	Biot's modulus	$M = 25.0$	GN/m ²
Lamé parameter	$G = 31.0$	GN/m ²	Biot's coefficient	$b = 0.5$	–
hardening modulus	$h = 5.0$	MN/m ²	fluid dyn. viscosity	$\eta_f = 1.0 \cdot 10^{-3}$	Ns/m ²
saturated yield shift	$\sigma_y = 0.1$	MN/m ²	permeability	$K = 9.8 \cdot 10^{-12}$	m ³ s/kg
saturation	$\omega = 2.0$	–	fluid density	$\rho_f = 1000.0$	kg/m ³
plastic viscosity	$\eta_p = 5 \cdot 10^{-6}$	s	crit. fracture energy	$\psi_c = 5.0 \cdot 10^{-8}$	MN/m ²
perturbation param.	$q_1 = 2 \cdot 10^{-5}$	MN/m ²	length scale	$l = 0.5$	m
slope yield function	$M_\phi = 1.8$	–	residual stiffness	$k = 1 \cdot 10^{-5}$	–
position of peak	$s_{\max} = 2 \cdot 10^{-3}$	MN/m ²	interpolation param.	$\epsilon = 50$	–

5.2 Comparison of different fracture driving forces for porous-elastic-plastic fracturing

In the present example, we investigate the influence of the presented fracture driving forces defined in (53) and (56). For that purpose, a squared domain with the dimensions of 80 m \times 80 m and a notch of the length $a = 8$ m in its center is considered, see Figure 10. The fracture evolution is triggered by fluid injection into the notch.

Due to the symmetry of loading and geometry only one half of the domain is discretized with 12,060 quadrilateral Raviart–Thomas-type enhanced-assumed-strain elements. The elements in the area surrounding the anticipated crack are refined yielding an element size of $h^e = 0.25$ m in that region ($[0 \text{ m}, 40 \text{ m}] \times [31.875 \text{ m}, 48.125 \text{ m}]$ around the notch).

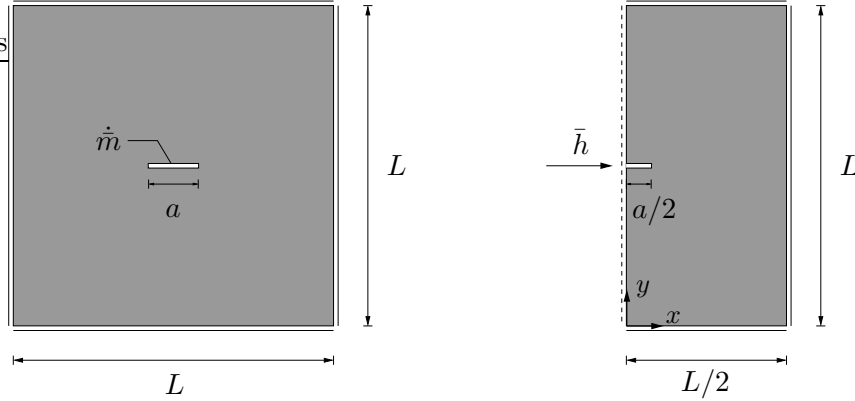


Figure 10: Comparison of different fracture driving forces: Geometry and boundary conditions. Due to the symmetry of both only one half of the specimen is discretized. Here the prescribed flux is $\bar{h} = \dot{m} = 0.01$ kg/s. All edges are mechanically fixed and permeable.

The fluid injection is modeled by a prescribed fluid flux of $\bar{h} = 0.01 \frac{\text{kg}^3}{\text{s}}$. The time step is set to $\tau = 1 \cdot 10^{-3}$ s and the material parameters are listed in Table 2.

The test was performed for the following two undrained settings with different choices of fracture driving forces:

- i) porous-elastic-plastic material with $\mathcal{H} = f(\psi_{\text{eff}}^0, \psi_{\text{plast}}^0)$ according to (53)
- ii) porous-elastic-plastic material with $\mathcal{H} = f(\psi_{\text{eff}}^0, w_{\text{plast}})$ according to (56)

We now compare the hydraulically induced fracture lengths for the two porous-elastic-plastic settings. As can be observed in Figure 11, both driving forces lead to the evolution of cracks. The fracture evolution in consideration of the fracture driving force $\mathcal{H} = f(\psi_{\text{eff}}^0, \psi_{\text{plast}}^0)$ is however less prominent. Note that in that setting, only the elastic and hardening energies contribute to the fracture driving force. Thus, we would not obtain ductile fracture evolution in case of ideal plasticity with ($h = 0, \sigma_y = 0$; not investigated here). In particular the latter observation justifies the presented modification of the fracture driving force in (56).

5.3 Detailed analysis of hydraulically induced porous-elastic-plastic fracture

Finally, we investigate the ductile fracture evolution driven by an injected fluid in detail. The setup of the geometry and boundary conditions as well as the material parameters are taken from the previous example (please refer to Figure 10 and Table 2).

The test was performed for two kinds of undrained materials:

- i) porous-elastic material
- ii) porous-elastic-plastic material with $\mathcal{H} = f(\psi_{\text{eff}}^0, w_{\text{plast}})$.

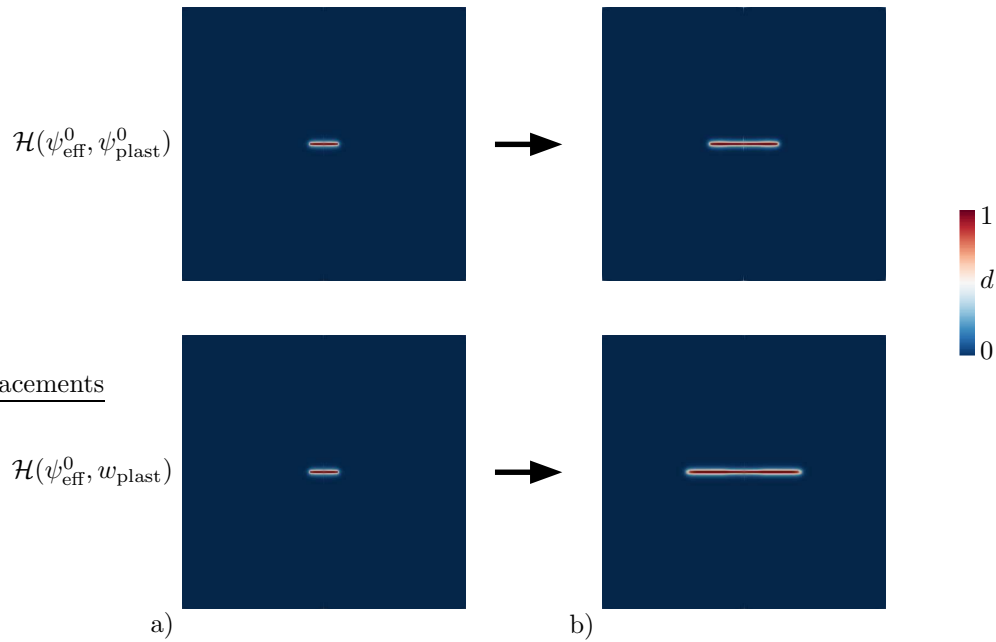


Figure 11: Comparison of different fracture driving forces: Distribution of the fracture phase-field for a porous-elastic-plastic with $\mathcal{H} = f(\psi_{\text{eff}}^0, \psi_{\text{plast}}^0)$ and a porous-elastic-plastic material with $\mathcal{H} = f(\psi_{\text{eff}}^0, w_{\text{plast}})$ at two time steps: a) $t = 0$ s and b) $t = 90$ s.

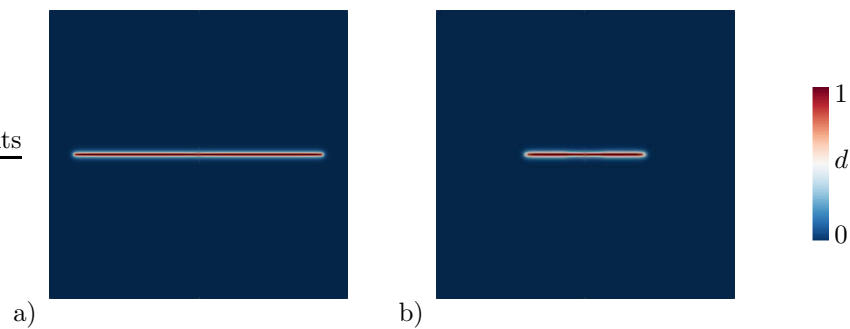


Figure 12: Hydraulically induced ductile fracture: Distribution of the fracture phase-field in a) porous-elastic material in b) porous-elastic-plastic material at $t = 90$ s.

As can be seen in Figure 12, the length of the finally induced crack for the porous-elastic material is much more pronounced than in case of the porous-elastic-plastic material. This goes along with the observation of a higher fluid pressure inside the crack, see Figure 13. We conclude that in case of an elastic-plastic material more fluid needs to be injected into the crack to drive fracturing. For the elastic material we can observe a characteristic drop of the pressure within the fracture at the onset of fracture propagation (injected fluid volume $V \approx 0.00004 \text{ m}^3$). In the elastic-plastic material this drop cannot be observed, see again Figure 13.

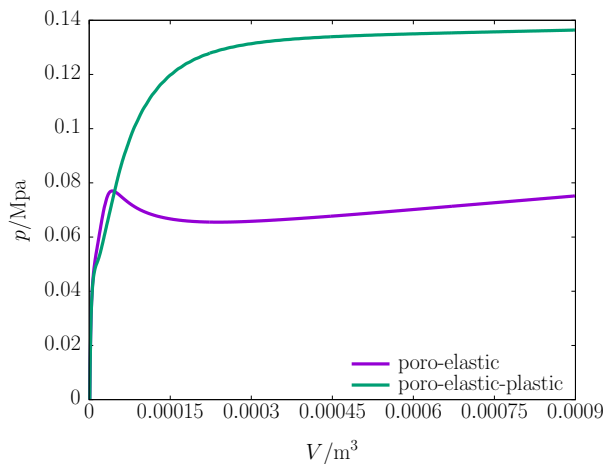


Figure 13: Hydraulically induced ductile fracture: Fluid pressure within the fracture at $x = 1.0 \text{ m}$, $y = 39.875 \text{ m}$ over inject volume for porous-elastic and porous-elastic-plastic material.

In Figure 14 the distribution of the change of the elastic fluid content is shown for the final equilibrium state. The individual lengths of the cracks are clearly visible. Due to the short crack length in the elastic-plastic case, the injected fluid is distributed over a smaller region. This then gives rise to a higher change of the elastic fluid content, in particular close to the fracture center. Note carefully that the change of the elastic fluid content in front of the fracture tips is negative for the elastic-plastic material. This phenomenon is investigated in a more detailed way in Figure 15, where the contributions of the change of the fluid content in the elastic-plastic material are shown.

By taking a look at Figure 15c, it can be seen that most of the volumetric plastic deformation occurs at the fracture tips ($\dot{m}^p = \rho_f b \text{tr } \dot{\epsilon}^p$). This leads to a positive change of the plastic fluid content. Since the permeability in the bulk is comparably low, very little amount of fluid diffuses from the fracture into the bulk. In other words, the change of the fluid content at the fracture tips is almost zero. Due to the definition $m = m^e + m^p$ the positive change of the plastic fluid content leads to a negative change of elastic fluid content. Hence the fluid in the fully saturated medium, which is initially stored elastically, is now stored plastically due to the plastic deformation of the solid matrix.

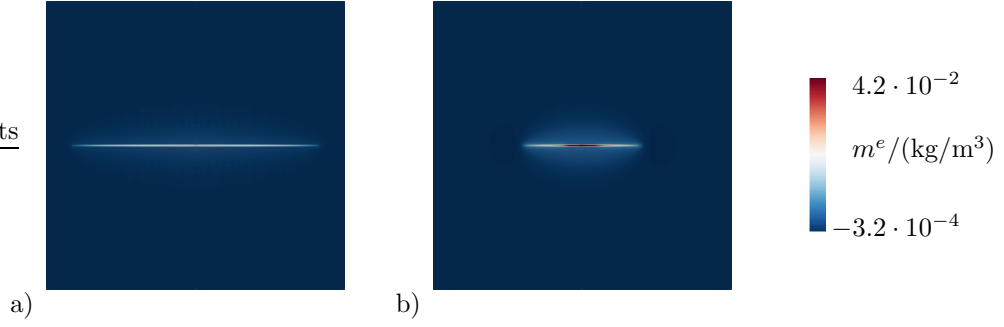


Figure 14: Hydraulically induced ductile fracture: Change of elastic fluid content m^e for porous-elastic material in a) and porous-elastic-plastic material in b).

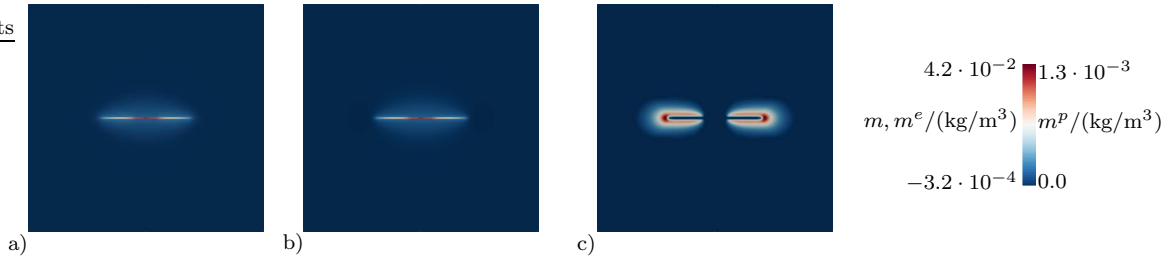


Figure 15: Hydraulically induced ductile fracture: Change of total fluid content m in a), change of elastic fluid content m^e in b) and change of plastic fluid content m^p in c) for porous-elastic-plastic material.

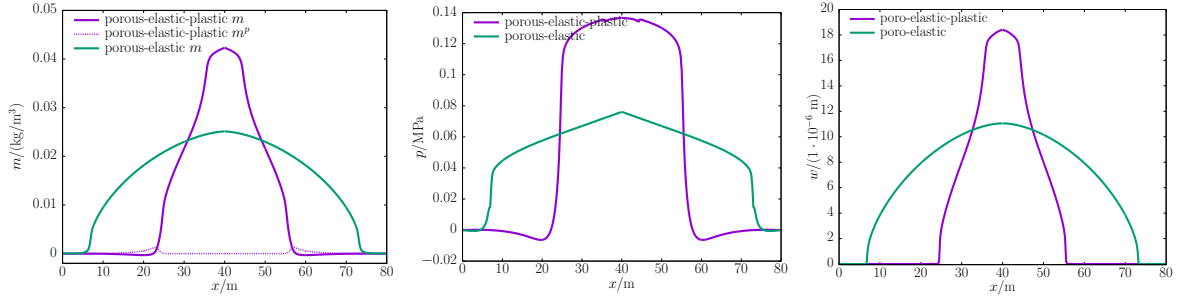


Figure 16: Hydraulically induced ductile fracture: Change of fluid content m and m^p , fluid pressure p and fracture opening w for porous-elastic and porous-elastic-plastic material over x at $y = 40$ m.

In Figure 16 we show the distribution of the change of fluid content as well as the pressure and the fracture-opening width along x at $y = 40$ m. These distributions refer to the final equilibrium state for both the porous-elastic and the porous-elastic-plastic material. The difference in the crack length for the two different materials and the positive change of the plastic fluid content as well as the negative change of the elastic fluid content in front of the fracture tip in the elastic-plastic material can again be observed.

Finally, we depict a sequence of three snapshots in the course of the fracture evolution of the porous-elastic-plastic material in Figure 17. To be specific, we show the fracture phase field across the whole domain together with the change of fluid content, the pressure

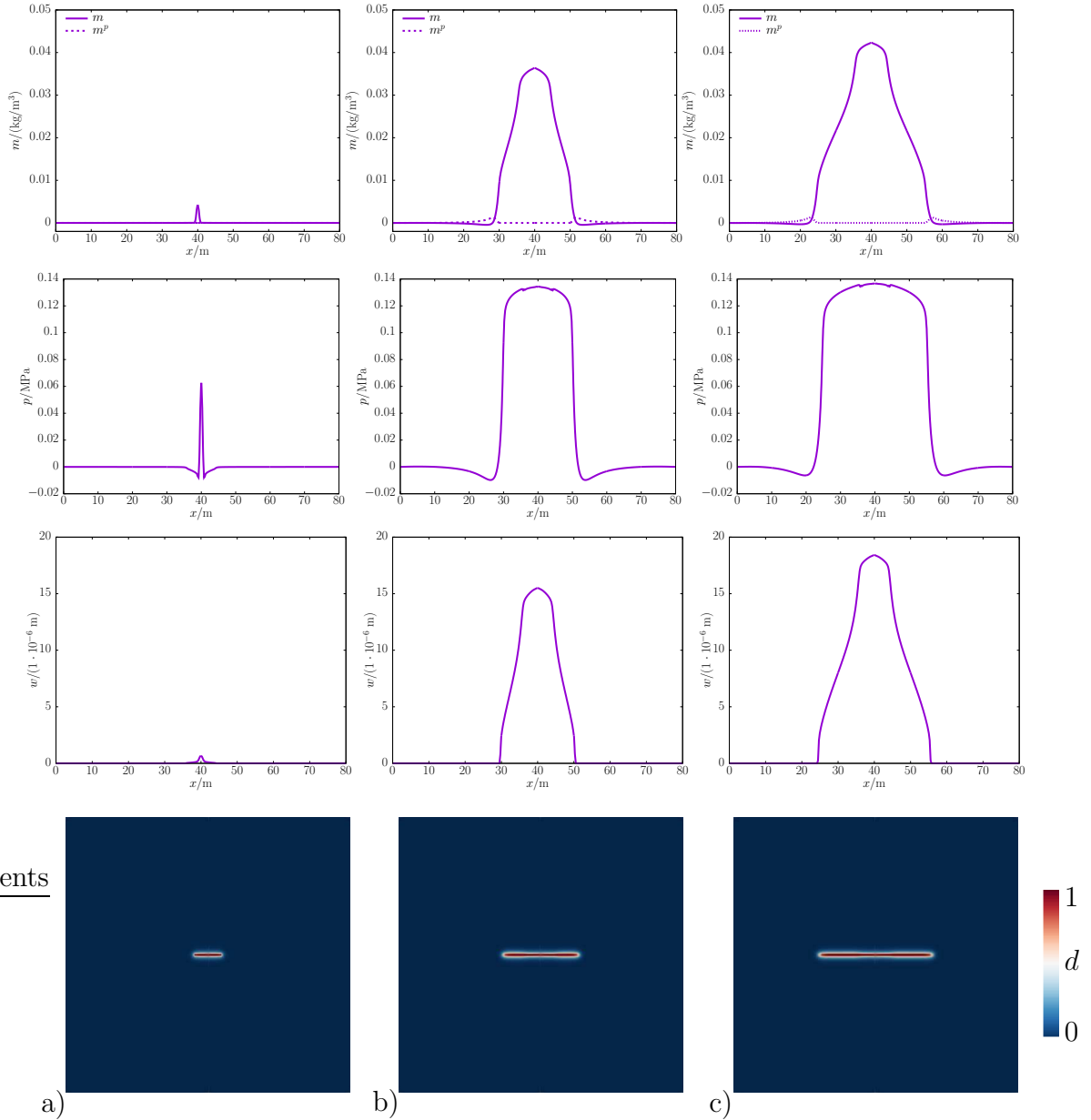


Figure 17: Hydraulically induced ductile fracture: Distribution of the fracture phase field and change of fluid content m and m^p , fluid pressure p and fracture opening w over x at $y = 40$ m for three different time steps: a) $t = 0$ s, b) $t = 45$ s and c) $t = 90$ s.

and the fracture-opening width at three different time steps along x at $y = 40$ m. The first time step is at $t = 0$ s, the second time step is at $t = 45$ s and the third time step is at the final state ($t = 90$ s). As can be seen, all considered quantities are mainly concentrated in the center of the fracture. Such a concentration is less prominent in case of an elastic material, see Figure 16.

6 Conclusion

A model for hydraulically induced fracturing in porous-elastic-plastic solids was developed in the present work. It incorporates a phase-field approach to fracture that is combined with a Drucker–Prager-type plasticity formulation and a Darcy–Biot-type fluid model. The model exploits a variational structure leading to a global minimization formulation. For this variational formulation it is crucial to introduce a plastic fluid content as an additional unknown yielding a constitutive fluid pressure in terms of only the elastic quantities. The global minimization structure demands the use of an $H(\text{div})$ -conforming finite-element formulation, which has been implemented by means of Raviart–Thomas-type shape functions. The locking phenomenon of the plasticity formulation is overcome by using an enhanced-assumed-strain formulation for the deformation.

In the first numerical example a comparison of an undrained porous-elastic, an undrained porous-elastic-plastic and a drained elastic-plastic formulation was performed. Here, the different physical effects were investigated. It could be shown that the permeability of porous media can be considered as an additional hardening parameter. The second example shows the effect of the proposed modification of the fracture driving force. In the third example, a hydraulically induced crack in a porous-elastic and a porous-elastic-plastic medium was investigated. There it could be shown that neglecting the plastic effects underestimates the pressure inside the fracture and overestimates the fracture length.

Acknowledgments. This work was funded by the Deutsche Forschungsgemeinschaft (DFG, German Research Foundation) – Project Number 327154368 – SFB 1313. This funding is gratefully acknowledged.

References

- Aldakheel, F., Noii, N., Wick, T., Wriggers, P., [2020]. *A global-local approach for hydraulic phase-field fracture in poroelastic media*. arXiv preprint arXiv:2001.06055.
- Alessi, R., Marigo, J.-J., Maurini, C., Vidoli, S., [2018a]. *Coupling damage and plasticity for a phase-field regularisation of brittle, cohesive and ductile fracture: One-dimensional examples*. International Journal of Mechanical Sciences 149, 559–576.
- Alessi, R., Vidoli, S., De Lorenzis, L., [2018b]. *A phenomenological approach to fatigue with a variational phase-field model: The one-dimensional case*. Engineering Fracture Mechanics 190, 53–73.
- Ambati, M., Gerasimov, T., De Lorenzis, L., [2015]. *Phase-field modeling of ductile fracture*. Computational Mechanics 55, 1017–1040.

- Amor, H., Marigo, J., Maurini, C., [2009]. *Regularized formulation of the variational brittle fracture with unilateral contact: Numerical experiments*. Journal of the Mechanics and Physics of Solids 57, 1209–1229.
- Armero, F., [1999]. *Formulation and finite element implementation of a multiplicative model of coupled poro-plasticity at finite strains under fully saturated conditions*. Computer Methods in Applied Mechanics and Engineering 171 (34), 205–241.
- Bear, J., [1972]. *Dynamics of Fluids in Porous Media*. Dover Publications, New York.
- Biot, M., [1941]. *General theory of three-dimensional consolidation*. Journal of applied physics 12, 155–164.
- Biot, M. A., [1984]. *New variational-lagrangian irreversible thermodynamics with application to viscous flow, reaction-diffusion, and solid mechanics*. Advances in applied mechanics. 24, 1–91.
- Bluhm, J., De Boer, R., [1997]. *The volume fraction concept in the porous media theory*. ZAMM-Journal of Applied Mathematics and Mechanics/Zeitschrift für Angewandte Mathematik und Mechanik 77 (8), 563–577.
- Borden, M. J., Hughes, T. J. R., Landis, C. M., Anvari, A., Lee, I. J., [2016]. *A phase-field formulation for fracture in ductile materials: Finite deformation balance law derivation, plastic degradation, and stress triaxiality effects*. Computer Methods in Applied Mechanics and Engineering 312, 130–166.
- Bourdin, B., Francfort, G. A., Marigo, J.-J., [2000]. *Numerical experiments in revisited brittle fracture*. Journal of the Mechanics and Physics of Solids 48, 797–826.
- Bourdin, B., Francfort, G. A., Marigo, J.-J., [2008]. *The Variational Approach to Fracture*. Springer.
- Cajuhi, T., Sanavia, L., De Lorenzis, L., [2018]. *Phase-field modeling of fracture in variably saturated porous media*. Computational Mechanics 61 (3), 299–318.
- Carrara, P., Ambati, M., Alessi, R., De Lorenzis, L., [2020]. *A framework to model the fatigue behavior of brittle materials based on a variational phase-field approach*. Computer Methods in Applied Mechanics and Engineering 361, 112731.
- Darcy, H., [1856]. *Les fontaines publiques de la ville de Dijon*. Dalmont, Paris.
- de Boer, R., [2000]. *Theory of Porous Media*. Springer, Berlin.
- Detournay, E., Cheng, A. H.-D., [1993]. *Fundamentals of poroelasticity*. In: Fairhurst, C. (Ed.), *Comprehensive Rock Engineering: Principles, Practice and Projects, Vol. II, Analysis and Design Method*. Pergamon Press, Ch. 5, pp. 113–171.
- Drucker, D. C., Prager, W., [1952]. *Soil mechanics and plastic analysis or limit design*.

- Quarterly of applied mathematics 10 (2), 157–165.
- Ehlers, W., [2002]. *Foundations of multiphasic and porous materials*. In: Ehlers, W., Bluhm, J. (Eds.), *Porous Media: Theory, Experiments and Numerical Applications*. Springer-Verlag, Berlin, pp. 3–86.
- Ehlers, W., Luo, C., [2017]. *A phase-field approach embedded in the theory of porous media for the description of dynamic hydraulic fracturing*. Computer Methods in Applied Mechanics and Engineering 315, 348–368.
- Ehlers, W., Luo, C., [2018a]. *A phase-field approach embedded in the theory of porous media for the description of dynamic hydraulic fracturing, part ii: The crack-opening indicator*. Computer Methods in Applied Mechanics and Engineering 341, 429–442.
- Ehlers, W., Luo, C., [2018b]. *A phase-field approach embedded in the theory of porous media for the description of dynamic hydraulic fracturing, part ii: The crack-opening indicator*. Computer Methods in Applied Mechanics and Engineering 341, 429–442.
- Francfort, G. A., Marigo, J.-J., [1998]. *Revisiting brittle fracture as an energy minimization problem*. Journal of the Mechanics and Physics of Solids 46, 1319–1342.
- Griffith, A. A., [1921]. *The phenomena of rupture and flow in solids*. Philosophical transactions of the royal society of london. Series A, containing papers of a mathematical or physical character, 163–198.
- Heider, Y., Markert, B., [2017]. *A phase-field modeling approach of hydraulic fracture in saturated porous media*. Mechanics Research Communications 80, 38–46.
- Irwin, G. R., [1958]. *Fracture*. In: Flügge, S. (Ed.), *Encyclopedia of Physics*. Vol. 6, Elasticity and Plasticity. Springer, pp. 551–590.
- Johnson, E., Cleary, M. P., et al., [1991]. *Implications of recent laboratory experimental results for hydraulic fractures*. In: *Low permeability reservoirs symposium*. Society of Petroleum Engineers.
- Kienle, D., Aldakheel, F., Keip, M.-A., [2019]. *A finite-strain phase-field approach to ductile failure of frictional materials*. International Journal of Solids and Structures 172, 147–162.
- Kuhn, C., Müller, R., [2010]. *A continuum phase field model for fracture*. Engineering Fracture Mechanics 77, 3625–3634.
- Lambrecht, M., Miehe, C., [2001]. *A note on formulas for localized failure of frictional materials in compression and biaxial loading modes*. International Journal for Numerical and Analytical Methods in Geomechanics 25, 955–971.
- Li, B., Peco, C., Millán, D., Arias, I., Arroyo, M., [2015]. *Phase-field modeling and simulation of fracture in brittle materials with strongly anisotropic surface energy*. Interna-

- tional Journal for Numerical Methods in Engineering 102 (3-4), 711–727.
- Lo, Y.-S., Borden, M. J., Ravi-Chandar, K., Landis, C. M., [2019]. *A phase-field model for fatigue crack growth*. Journal of the Mechanics and Physics of Solids 132, 103684.
- Mauthe, S., Miehe, C., [2017]. *Hydraulic fracture in poro-hydro-elastic media*. Mechanics Research Communications 80, 69–83.
- Miehe, C., [1998]. *A formulation of finite elastoplasticity based on dual co- and contra-variant eigenvector triads normalized with respect to a plastic metric*. Computer Methods in Applied Mechanics and Engineering 159, 223–260.
- Miehe, C., Aldakheel, F., Raina, A., [2016a]. *Phase field modeling of ductile fracture at finite strains. a variational gradient-extended plasticity-damage theory*. International Journal of Plasticity 84, 1–32.
- Miehe, C., Hofacker, M., Schänzel, L.-M., Aldakheel, F., [2015a]. *Phase field modeling of fracture in multi-physics problems. Part II. brittle-to-ductile failure mode transition and crack propagation in thermo-elastic-plastic solids*. Computer Methods in Applied Mechanics and Engineering 294, 486–522.
- Miehe, C., Hofacker, M., Welschinger, F., [2010a]. *A phase field model for rate-independent crack propagation: Robust algorithmic implementation based on operator splits*. Computer Methods in Applied Mechanics and Engineering 199, 2765–2778.
- Miehe, C., Kienle, D., Aldakheel, F., Teichtmeister, S., [2016b]. *Phase field modeling of fracture in porous plasticity: A variational gradient-extended eulerian framework for the macroscopic analysis of ductile failure*. Computer Methods in Applied Mechanics and Engineering 312, 3–50.
- Miehe, C., Mauthe, S., Teichtmeister, S., [2015b]. *Minimization principles for the coupled problem of darcy-biot-type fluid transport in porous media linked to phase field modeling of fracture*. Journal of the Mechanics and Physics of Solids 82, 186–217.
- Miehe, C., Teichtmeister, S., Aldakheel, F., [2016c]. *Phase-field modeling of ductile fracture: A variational gradient-extended plasticity-damage theory and its micromorphic regularization*. Philosophical Transactions of the Royal Society A 374.
- Miehe, C., Welschinger, F., Hofacker, M., [2010b]. *Thermodynamically consistent phase-field models of fracture: Variational principles and multi-field fe implementations*. International Journal for Numerical Methods in Engineering 83, 1273–1311.
- Mikelic, A., Wheeler, M. F., Wick, T., [2015a]. *A phase-field method for propagating fluid-filled fractures coupled to a surrounding porous medium*. Multiscale Modeling & Simulation 13 (1), 367–398.
- Mikelic, A., Wheeler, M. F., Wick, T., [2015b]. *A phase-field method for propagating*

-
- fluid-filled fractures coupled to a surrounding porous medium*. Multiscale Modeling & Simulation 13 (1), 367–398.
- Mikelic, A., Wheeler, M. F., Wick, T., [2015c]. *Phase-field modeling of a fluid-driven fracture in a poroelastic medium*. Computational Geosciences, Springer Verlag (Germany).
- Pham, K., Amor, H., Marigo, J.-J., Maurini, C., [2011]. *Gradient damage models and their use to approximate brittle fracture*. International Journal of Damage Mechanics 20 (4), 618–652.
- Pise, M., Bluhm, J., Schröder, J., [2019]. *Elasto-plastic phase-field model of hydraulic fracture in saturated binary porous media*. International Journal for Multiscale Computational Engineering 17 (2).
- Raviart, P. A., Thomas, J. M., [1977]. *Primal hybrid finite element methods for 2nd order elliptic equations*. Mathematics of computation 31 (138), 391–413.
- Schreiber, C., Kuhn, C., Müller, R., Zohdi, T., [2020]. *A phase field modeling approach of cyclic fatigue crack growth*. International Journal of Fracture, 1–12.
- Simo, J. C., Rifai, S., [1990]. *A class of mixed assumed strain methods and the method of incompatible modes*. International Journal for Numerical Methods in Engineering 29, 1595–1638.
- Steinke, C., Zreid, I., Kaliske, M., [2020]. *Modelling of ductile fracture of strain-hardening cement-based composites-novel approaches based on microplane and phase-field method*. In: *Plasticity, Damage and Fracture in Advanced Materials*. Springer, pp. 175–199.
- Storm, J., Supriatna, D., Kaliske, M., [2020]. *The concept of representative crack elements for phase-field fracture: Anisotropic elasticity and thermo-elasticity*. International Journal for Numerical Methods in Engineering 121 (5), 779–805.
- Teichtmeister, S., Kienle, D., Aldakheel, F., Keip, M.-A., [2017]. *Phase field modeling of fracture in anisotropic brittle solids*. International Journal of Non-Linear Mechanics 97, 1–21.
- Teichtmeister, S., Mauthe, S., Miehe, C., [2019]. *Aspects of finite element formulations for the coupled problem of poroelasticity based on a canonical minimization principle*. Computational Mechanics 64 (3), 685–716.
- Terzaghi, K., [1925]. *Erdbaumechanik auf bodenphysikalischer Grundlage*. F. Deuticke.
- Vermeer, P., de Borst, R., [1984]. *Non-associated plasticity for soils, concrete and rock*. Heron 29 (3), 1–64.
- Wilson, Z. A., Landis, C. M., [2016]. *Phase-field modeling of hydraulic fracture*. ICES Report 16-10.

- Wu, T., De Lorenzis, L., [2016]. *A phase-field approach to fracture coupled with diffusion*. Computer Methods in Applied Mechanics and Engineering 312, 196–223.
- Yin, B., Kaliske, M., [2020]. *A ductile phase-field model based on degrading the fracture toughness: Theory and implementation at small strain*. Computer Methods in Applied Mechanics and Engineering 366, 113068.